

TESI DI DOTTORATO

UNIVERSITÀ DEGLI STUDI DI NAPOLI "FEDERICO II"

DIPARTIMENTO DI INGEGNERIA BIOMEDICA ELETTRONICA E
DELLE TELECOMUNICAZIONI

DOTTORATO DI RICERCA IN INGEGNERIA ELETTRONICA E DELLE
TELECOMUNICAZIONI

POROUS MEDIA CHARACTERIZATION
BY MICRO-TOMOGRAPHIC
IMAGE PROCESSING

MARCELLA MATRECANO

Il Coordinatore del Corso di
Dottorato

Ch.mo Prof. Niccolò RINALDI

Tutore

Ch.mo Prof. Giovanni POGGI

A. A. 2010-2011

Contents

Contents	I
List of Figures	III
Abstract	VI
Acknowledgements	VIII
Introduction	IX
Aim of the research	X
Typical workflow in image processing for porous systems	XII
Structure of the thesis and innovation	XIII
Porous media imaging techniques	1
1.1. Laboratory X-ray micro-CT	4
1.1.1. Fundamentals	5
1.1.2. Reconstruction from projections	8
1.2. Issues in CT imaging	14
1.2.1. Noise	15
1.2.2. Reconstruction artifacts	16
Morphology approach on image analysis for porous media	19
2.1. Porous media image analysis objectives	21
2.1.1. Geo-Sciences applications	21
2.1.2. Biomedical applications	25
2.2. The morphological approach	29
2.2.1. Some basic concepts	30
2.2.2. The “Successive Openings” algorithm	35
2.2.3. A fast implementation	41

2.3.	Quantification of features	47
2.3.1.	Dimensional curve	48
2.3.2.	Connectivity curve	51
2.3.3.	Effective porosity identification	57
2.4.	Advances in geo-sciences	62
2.4.1.	Experimental results	63
2.5.	Advances in biology	73
2.5.1.	Experimental results	73
	Image denoising	79
3.1.	CT noise	80
3.1.1.	Noise experimental characterization	81
3.1.2.	CT image denoising: state of art	86
3.2.	State of the art of non-AWGN denoising techniques	89
3.3.	The modified BM3D algorithm	91
3.4.	Results	94
	Conclusion	99
	References	101

List of Figures

Figure 1.1: Electromagnetic spectrum.	1
Figure 1.2: Scheme of an x-ray tube.	6
Figure 1.3: Schematic of x-ray tube spectrum.	6
Figure 1.4: Contribution of each voxel to the total x-ray absorption along rays.	8
Figure 1.5: Back projection example for a square object.	10
Figure 1.6: Tomographic reconstruction using backprojection.	11
Figure 1.7: Tomographic reconstruction using filtered backprojection.	12
Figure 1.8: Relationship between the profile measured in the spatial domain and the corresponding representation in the frequency domain.	13
Figure 1.9: Cone beam geometry.	14
Figure 1.10: Schematic view of ring artifact.	17
Figure 2.1: Two-dimensional illustration of medial axis determination.	24
Figure 2.2: An illustration of the difficulty in determining single pore bodies.	25
Figure 2.3: Illustration of a long bone showing the diaphysis, epiphyses, medullary cavity, cortical and trabecular bone.	26
Figure 2.4: Mean intercept length. The number of bone-marrow interfaces is counted along the parallel lines through the specimen for different angles θ	28
Figure 2.5: Some 2D structuring elements, a) square, b) cross, c) circle, d) line.	30
Figure 2.6: <i>Erosion</i> of A by structuring element B	31
Figure 2.7: <i>Erosion</i> of A by circular structuring element B	32
Figure 2.8: <i>Dilation</i> of A by rectangular structuring element B	33
Figure 2.9: <i>Dilation</i> of A by circular structuring element B	33
Figure 2.10: <i>Opening</i> of A by circular structuring element B	34

Figure 2.11: Algorithm flowchart	36
Figure 2.12: Incomplete SE subset with increasing diameters. 37	
Figure 2.13: Effect of <i>Opening</i> with circular SE of radius $r=3$.37	
Figure 2.14: Effect of <i>Opening</i> with circular SE of radius $r=5$. 38	
Figure 2.15: Effect of <i>Opening</i> with circular SE of radius $r=15$	39
Figure 2.16: Effect of <i>Opening</i> with circular SE of radius $r=25$	39
Figure 2.17: Effect of <i>Opening</i> with circular SE of radius $r=35$	40
Figure 2.18: Alternative algorithm flowchart.	46
Figure 2.19: (a) O_{11} image; (b) sum of G_i functions.....	47
Figure 2.20: A binary image, on the left, and its dimensional curve, on the right.	50
Figure 2.21: A 2D image and its dimensional curve for only six macro-classes.	50
Figure 2.22: Representation of VOI in 3D.....	52
Figure 2.23: Proximity configuration: (a) N_6 , (b) N_{18} , (c) N_{26} ..	53
Figure 2.24: Connectivity algorithm flowchart.	54
Figure 2.25: (a) Original image; (b) connected components from top to bottom	55
Figure 2.26: (a) Image of connected objects after <i>opening</i> with $r=5$; (b) image of connected objects after <i>opening</i> with $r=10$	56
Figure 2.27: Percolation curve of a 2D example image.....	56
Figure 2.28: <i>Hit or Miss</i> template $B=(B_1, B_2)$	58
Figure 2.29: Thinning (left); pruning (right).....	59
Figure 2.30: (a) Input signal, (b) initial flooding, (c) a dam is created when water from different minima is ready to merge, (d) final flooding.	60
Figure 2.31: (a) Z -connected volume, (b) skeleton.	61
Figure 2.32: (a) Z -connected volume segmented by watershed lines, (b) effective porosity volume.	62
Figure 2.33: Visualisation of the solid and pore phase of the three samples at 10 micron image resolution. Volumes are cubes with side of 3.5mm.	64

Figure 2.34: Pore size distribution of the three samples computed by “successive <i>opening</i> ”. Porosity under one voxel has not been taken into account.....	65
Figure 2.35: Horizontal and vertical pore connectivity (>10 microns) evaluated by the “percolation curve”.....	65
Figure 2.36: Experimental (pink) and trend (gray) execution time for LC sample.	67
Figure 2.37: CPU time for the three versions of “successive openings”.	68
Figure 2.38: PoSD curve of an LC sample obtained by three different algorithms.....	69
Figure 2.39: Soil crust samples, T1, T2 and T3.....	70
Figure 2.40: Soils reconstructions.....	70
Figure 2.41: PoSD comparison.....	71
Figure 2.42: 3D PoSD comparison.	71
Figure 2.43: Pore network skeleton.	72
Figure 2.44: Tortuosity comparison.....	72
Figure 2.45: TrSD comparison.	74
Figure 2.46: ‘Sample A’ connectivity curve.....	76
Figure 2.47: ‘Sample B’ connectivity curve.	77
Figure 3.1: Test object reconstructed image.....	83
Figure 3.2: Selected square ROI.....	83
Figure 3.3: The gray level distribution of the mean image.....	84
Figure 3.4: (a) Image of noise, (b) relative frequencies distribution of the pixels gray levels, in blue, and normal pmf, in red.....	85
Figure 3.5: Correlation coefficient variation along the rows and columns.	85
Figure 3.6: Visual results for a crop-outs of House.....	97
Figure 3.7: Visual results for a crop-outs of Flinstone.	98

Abstract

In this thesis, we have focused our attention on the characterization of porous media through micro-tomographic image processing.

A porous medium can be simply seen as a solid material with "holes" in it, which, connected or isolated, may or may not eventually allow the flow of one or more fluids. They have various applications in common practice and are widely used in many disciplines, both scientific and industrial. Porous media are strongly characterized by their internal microstructure, which needs to be accurately described in order to determine their performance and macroscopic properties. Despite recent technological advances and the introduction of imaging techniques such as X-ray micro-tomography, methods to characterize quantitatively the porous media internal structure are still few and related to some specific applications.

To this regards, we propose new algorithms for the analysis of the 3D micro-architecture of porous media based on image processing and the mathematical morphology theory. In particular, the *opening* operator properties have been exploited in the "successive openings" algorithm which represents the starting point for the construction of three morphological synthetic indicators. They are the dimensional curves, Pore Size Distribution (PoSD) and Trabecular Size Distribution (TrSD), which provide information about the pores or solid phase structure, the connectivity curves, which allow to identify how the structural elements are interconnected, and the effective porosity, which represents the porous fraction concerned with the transport of fluids. Experimental results show that the proposed indicators together represent an effective tool for the porous media internal structure characterization.

Since noise is a primary cause of reduced image analysis capability in micro-CT, we have dedicated a part of our research to the reduction of the strong noise that corrupts tomographic images. After evaluating experimentally the characteristics of noise, we propose a filtering technique for correlate noise based on the *Block-Matching 3D* (BM3D) algorithm. Experimental results prove the proposed technique effectiveness and its potential to improve the performance of the algorithms proposed in the first part.

Although micro-tomographic image processing presents considerable difficulties, both for the intrinsic characteristics of the images, and for the nature of analyzed objects, this thesis proves that reliable and useful indications about the structure of porous media can be obtained through the use of the mathematical morphology theory.

Acknowledgements

I would like to express my sincere gratitude to my supervisors Professor Giovanni Poggi (Department of Biomedical Electronic and Telecommunication Engineering) for giving me the opportunity to undertake my PhD. In particular, I would like to thank Annalisa, Sara P., Mariana, Vincenzo, Tommaso, Giulio and Sara C., for their support, friendship and enthusiasm. To you I will be forever grateful.

I would like to thank my family and friends who have supported me during this time and motivated me at times when my own motivation was lacking. I would especially like to thank my parents and Alfonso. I love you. Thank you.

I would like to thank staff of the CNR “ISAFOM” centre of Ercolano (Naples, Italy) for their expertise, advice and many stimulating discussions both related and unrelated to this work. In particular, I would like to thank Ing. Giacomo Mele for all his assistance and advice.

I would like to thank Professor Mario Cesarelli (Department of Biomedical Electronic and Telecommunication Engineering) and researcher Maria Romano. Without your help this project simply would not happen. Thank you.

Introduction

Following a popular definition “a porous medium is a material consisting of a solid matrix with an interconnected void” [1]. The skeletal portion of the material is often called the matrix or frame and undergoes small deformation. The interconnectedness of the void (the pores) typically allows the flow of one or more fluids through the material, but the requirement of flow is not mandatory for the definition. In the simplest situation (single-phase flow) the void is saturated by a single fluid, while in two phase flow, a liquid and a gas share the void space. Therefore, in porous media, there can be two or more material constituent arranged in any disorderly fashion, but distinct interfaces should demarcate these constituents.

Porous media are more common and important than one might think. Many natural substances such as zeolites, rocks and soil (e.g., aquifers, petroleum reservoirs), biological tissues (e.g. bones, wood, cork), and man made materials such as cements, bread and ceramics can be considered as porous media. Many of their important properties can only be understood by considering them to be porous media. Indeed, porous media are studied in many areas of applied science and engineering: filtration, mechanics (acoustics, geomechanics, soil and rock mechanics), engineering (petroleum, bio-remediation, construction), geosciences (hydrogeology, petroleum geology, geophysics), biology and biophysics, material science, etc. Also the fluids that flow through porous media are subjects of common interest and this has emerged in a separate field of study.

A porous medium is most often characterized by its porosity and in particular by how its porosity is distributed. Other properties of the medium (e.g., permeability, tensile strength, electrical conductivity) can be connected to the

porosity or to the pore structure. For this reason, many efforts have been made in an attempt to characterize the internal structure of porous media and this is precisely the ultimate goal of our research.

Aim of the research

The solution of practical problems involving multiphase porous media or systems requires the knowledge of the porous matrix macroscopic properties. In fact, the geometric and morphological characterization of the porous media internal microstructure is essential for understanding their mechanical, acoustic, thermal or fluid-dynamic properties.

For example, the natural porous media observation plays a key role in the actual environmental issues such as contaminated aquifers restoration, geothermal energy production or carbon dioxide storage into the ground, and also in the petroleum engineering related problems. In all these cases, the description from a morphological, topological and geometrical point of view of the complex pore space is essential for the understanding fluid and heat transport phenomena through the medium.

Often in the past, specific analysis techniques have been applied to two-dimensional (2D) images obtained by optical methods, but they returned only partial information about the porous media structure. Increased computational power and progresses in imaging techniques are providing researchers with the tools and data to take a big leap ahead in understanding of media microstructure, but the extension from 2D analysis to three-dimensional (3D) case represents a non-trivial challenge, requiring both a large computing effort and new methodological approaches implementation.

In fact, despite their potential, 3D imaging techniques are often used only for qualitative assessment by visualization while

objective methods would be needed to directly quantify the void structure. One of the crucial points is the difficulty in transforming the large set of digital data into synthetic indicators that integrate useful information. Typically, researchers have to process a huge amount of data and therefore, analyze them in a quantitative, physically and representative manner is really challenging. In many cases, they have to exercise a significant effort to invent approaches and tools that are often applicable only within narrow circumstances of data type or computer configuration.

There is therefore a lack of methodology to study 3D structures, and there are very few software tools [2] [3] [4] [5], neither easily accessible nor generally purpose, that allow the extraction of quantitative information of interest.

In this thesis, we introduce, describe and utilize 3D image analysis procedures for porous media in order to supply a quantitative characterization of their inner structure, intended to fill part of this gap. In particular, we suggest a new approach to porous media microstructure analysis, based on mathematical morphology theory [6], which provides a set of techniques to study structures (objects) as images, widely applied to 2D images. We also propose some indicators which are able to characterize the 3D microstructure in a quantitative manner. In this way, and also through the implementation of 3D image analysis algorithms applied to the micro-tomographic images, we have found a greater correlation between the morphometric parameters proposed and the structural properties of porous media.

These procedures have been initially developed with the primary motivation of analyzing micro-tomographic images of soil samples, collected by the National Research Council (CNR) ISAFOM Institute of Ercolano. However, they are applicable generally to any three-dimensional data set containing identifiable discrete features; in fact we have also applied them to micro-tomographic data of bone.

The ultimate goal of this work is to provide an instrument to researchers for:

- analyze 3D samples in automatic way;
- find the distribution of the pore or the solid space;
- quantify porosity, volume, surface areas, connectivity and spatial distribution, and thus provide input for various formulae/estimates;
- predict: permeability, formation factor, elastic properties, etc;
- use pore and solid models for simulation.

Typical workflow in image processing for porous systems

To extract useful and reliable information, the image analysis algorithms proposed in this thesis need to address a broad spectrum of problems, typical of image processing and computer vision as well as specific of this field: enhancement, segmentation, statistical size distributions, connectivity analysis, correspondence between the features extracted from analyzed images and porous media characteristics. Although these steps represent a typical workflow in image processing for porous systems (see for example [7] [8] [9]), these procedures are far from being standardized, such as verified in [10], and all of these steps can be affected by artefacts or subjectivity.

First of all, before measurements can be performed, specimens need to be sampled, possibly dried in some way and eventually solidified by impregnation with one of a number of available resins. For every scanners used to generate three-dimensional data, the resolution of the scanning, and a number of settings related to attenuation and contrast, can differ, depending on who does the scanning. Finally, the resulting 3-D images are segmented into binary image, to which a wide range of analysis methods are then applied. All these steps involve operational decisions which may vary from one user to another.

From the above, it is clear that the comparison of proposed methods with other ones can sometimes be difficult or even meaningless, given the strong presence of the human factor, both in acquisition procedures, and in the processing and analysis. Despite this, some of the most common approaches to image analysis for porous media were considered in order to validate the contribution of the proposed techniques.

Structure of the thesis and innovation

Here, with reference to the appropriate chapters, we will briefly describe the innovative contribution of our work.

First of all, in Chapter 1 we introduce the micro-computed tomography, an imaging technique which produces images used in this thesis. Understanding the operating principles of this technique is important, because they determine the characteristics of images to be processed. Without this knowledge, we cannot deal correctly with the engineering challenges that this method present.

In Chapter 2 we first introduce the concepts of mathematical morphology, proposed by Serra in 1982 [6]. This is a branch of image analysis that offers a unified and powerful approach to numerous image processing problems. It is often used as a tool for extracting image components that are useful in the representation and description of region shape. These concepts are used as building blocks for assembling 3D processing procedures. Indeed, we explain a morphological analysis algorithm, called "successive openings". The algorithm allows us to determine some important synthetic indicators: dimensional curves, Pore Size Distribution (PoSD) and Trabecular Size Distribution (TrSD), which provide information about the pores or solid phase structure, the connectivity curves, which identify if the medium structural elements are interconnected and in that manner, and the effective porosity,

which represents the porous fraction concerned with the fluids transport.

Although the algorithm uses carefully and efficiently the potential of the developing environment MATLAB[®], its computation time is quite large, given the large volumes of data involved. For this reason it an alternative version has been also developed, based on the distance transform, which provides results almost identical but much faster. At the end of the chapter two applications are illustrated: one in the geology, with the application of the algorithm to soil samples, and another one in biomedical field, with reference to samples of bones.

In Chapter 3 we then deal with the reduction of the strong noise that corrupts tomographic images. After evaluating experimentally the characteristics of noise, we propose a filtering technique for correlate noise based on the *Block-Matching 3D* (BM3D) algorithm, which can be considered the state of the art for AWGN image denoising. Experimental results on test images, corrupted by different types of colored noise, prove the proposed technique effectiveness and its potential to improve the performance of the algorithms proposed in the Chapter 2.

In the conclusions, we comment results and discuss outstanding issues with a look at future research.

Chapter 1

Porous media imaging techniques

Nowadays, the principal energy source used for imaging is the electromagnetic (EM) energy spectrum, but other important sources are used, such as acoustic, ultrasonic and electronic signals.

Electromagnetic waves can be conceptualized as propagating, sinusoidal waves of varying wavelength (Figure 1.1). One could consider all probes as beams with energy and wavelength that interact differently with matter. Obviously, the wavelength required to “see” an object must be of the same size or smaller than the object.

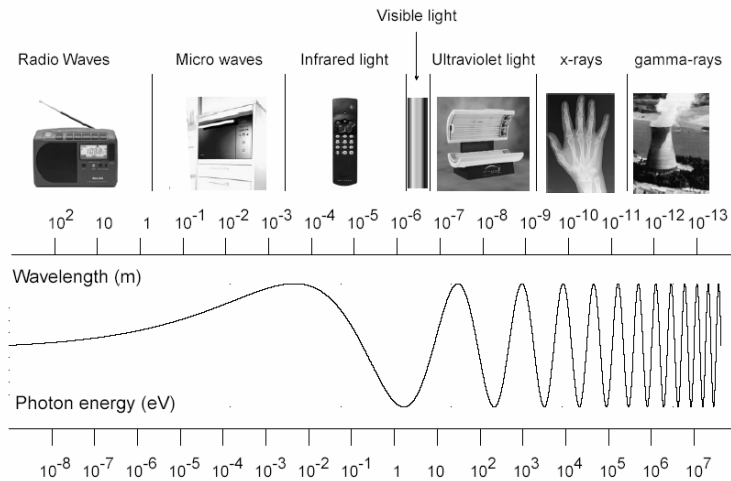


Figure 1.1: Electromagnetic spectrum.

Although the techniques that utilize electromagnetic energy could be very different they share similar concepts.

Every EM imaging relies on the ability to “illuminate” an object, and collect and analyze the radiation that it scatters or transmits. On the contrary, the opacity is a phenomenon not permitting the passage of electromagnetic radiation.

Until a few years ago, the study of porous media by image analysis was limited to destructive methods such as thin-sectioning, and the imaging techniques relying on those methods were inherently bi-dimensional (2D) [11]. Indeed, the three-dimensional information of object structures was obtained by cutting the object into very thin slices, which were visualized in the light microscope, then the two-dimensional information was interpolated into a three-dimensional (3D) structure model.

In most cases, however, an accurate analysis of the original three-dimensional object structure cannot be made on the base of two-dimensional information. In fact, this method is not only very cumbersome but also rather unreliable since the object structure itself can be altered by the preparation technique and the distance between the slices is usually too coarse to avoid loss of 3D information. Furthermore, due to the highly anisotropic organization of porous media, the evaluation of its 3D architecture based on 2D measures could conduct to wrong conclusions.

Thanks to the recent advances in technology it has been possible to switch to techniques that provide 3D images, such as Nuclear Magnetic Resonance (NMR), Focused Ion Beam-SEM (FIM), Transmission Electron Microscopy (TEM), Neutron Tomography and Computed Tomography (CT); or to improve the 2D ones, like for example the Confocal Laser Scanning Microscopy (CLSM) which, even if used only on single grains and not on 3D porous media, returns high quality images.

The passage from 2D to 3D brings many advantages. First of all, methods become non-destructive, allowing for measure repeatability. In addition, it is possible to directly observe the changes that take place inside a material, and hence

follow a process with no need of hypotheses on the media structure.

In this thesis work, we consider images from Computed Micro Tomography (microCT), so we will focus on this technique in the following, but for the sake of completeness, we shortly describe here some other commonly used techniques, referring the reader to specific texts for in-depth examination.

The Magnetic Resonance Imaging (MRI) techniques are based on the physics principle stating that hydrogen protons (from water molecules) align themselves with the main magnetic field. When a second magnetic field, orthogonal to the first, oscillates at radio frequencies, protons are pushed out of alignment and emit a detectable radio frequency signal as they return to align with the first field. Protons in different tissues (materials) realign at different speeds. This property is used to distinguish various materials that characterize the media. The MRI techniques are heavily used in medical imaging because they are non-destructive and because they utilize non-ionizing radio frequencies, but their resolution is limited and require long acquisition times [12].

FIB (Focused Ion Beam) is similar, in principle, to scanning electron microscope (SEM). However, instead of an electron beam, a finely focused ray of ions with a diameter down to approximately 5 nm is used here. Operating the primary ion beam at low currents allows the imaging of samples. At high currents, instead, significant material ablation is induced, enabling precise milling, cutting drilling and structuring at the nano-level [13].

The TEM is based on the same fundamental principles used by the light microscope, but utilizes electrons instead of light. TEMs use electrons as “light source” and, thanks to their shorter wavelength, it is possible to get resolutions a thousand times better than with a light microscope. TEM allows one to see objects in the order of a few angstrom (10^{-10} m), reaching atomic levels [14].

Neutron Radiology and Tomography are non-destructive imaging techniques utilizing thermal neutrons (a nuclear reactor

is necessary). The working principle is similar to x-ray CT but neutrons have many advantages for imaging over visible light, x-rays or electrons. They include greater penetration depth into most materials, considerable variations in contrast between chemical elements and isotopes, and high sensitivity to hydrogen. Unlike x-ray, neutron based CT is not nearly as well developed and it requires long exposure times [15].

However, among all the techniques, those based on x-rays are the most widespread since they are non destructive, fast and reach good resolutions (down to 1-5 μm). Moreover, they are highly developed and commercialized.

1.1. Laboratory X-ray micro-CT

X-ray computed tomography¹ is an imaging method where individual projections (radiographs), recorded from different viewing directions, are used to reconstruct the internal structure of the object of interest. X-ray CT is quite familiar in its medical application, but it is not so commonly considered as an imaging modality for components or materials. Nevertheless, its ability to visualize the three-dimensional structure of objects, often without sample preparation or chemical fixation, makes it an ideal tool for the study of porous media. In particular, the micro-computed tomography systems can be considered as high-resolution version of the CT medical scanners. They have been developed at a slower rate than the latter, because they have not found immediate clinical application, but are used above all in research. The microCT systems began to grow in number in mid-to-late 1990s [16] when common practice became to study human disease carrying out experiments on animals, and therefore their cost has decreased a lot.

¹ The word tomography arises from the Greek *tomos* for “section or cut”, and *graphein* for “to write”.

The division between conventional CT and microCT is, of course, an artificial distinction and is strictly linked to the resolution. It describes how well small details can be imaged and located with respect to some reference points, and it depends on the ability to focus or collimate the probe, generally limited to the wavelength. Typically, the spatial resolution of conventional medical CT-scanners is in the range of 1 – 2,5 mm, which corresponds to voxels (volume elements) of 1 – 10 cubic mm. MicroCT gives the possibility to improve this spatial resolution by seven to eight orders of magnitude in terms of volume, depending on the application. Indeed, the actual resolution needed relates to the type and shape of the micro-structural features of interest. Therefore, the development of CT devices in the medical field has been conditioned by the several constraints due to their use on patients. First, the dose of x-rays received by the patient must be kept to a minimum, because its toxicity. Second, the acquisition time can last only few seconds, to prevent involuntary patient movements (e.g., breath, tremor, etc.) that could degrade the image quality. In general, these constraints do not apply for the imaging of inanimate objects, where the possibility of extending the exposure time, and then the dose, is used to improve the signal-to-noise ratio in the data.

Nowadays, the micro-CT is widely used in many fields including: electronic, biology, geology, materials science, food industry, oil and semiconductor industry, archaeology and biomedical engineering. The application of microCT to biomedical and environmental science problems is the main topic of this thesis.

1.1.1. Fundamentals

The details of x-ray generation and interaction with matter are covered only briefly in this section because this is beyond the scope of this work. Further details can be found in specialized texts [17].

1.1.1.1. X-rays generation

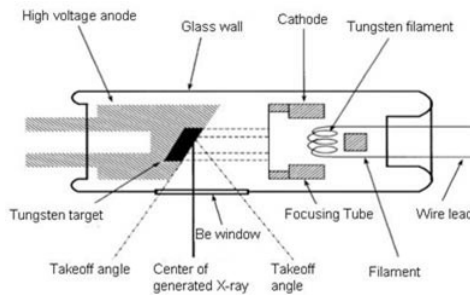


Figure 1.2: Scheme of an x-ray tube.

In a tomographic system, an X-ray source consists in an tube, in which the electrons emitted from a cathode, are first accelerated by an electric potential difference and then sharply braked during a collision with an heavy metal anode (generally a metal such as Cu, Mo, Ag, or W).

Upon striking the target, the electrons are decelerated and produce a radiation consisting in a continuous component added to a discrete one (characteristic emission of the anode material), see Figure 1.3. Only a very small fraction of the energy of the electron beam is converted to x-radiation; most of the energy is instead released as heat.

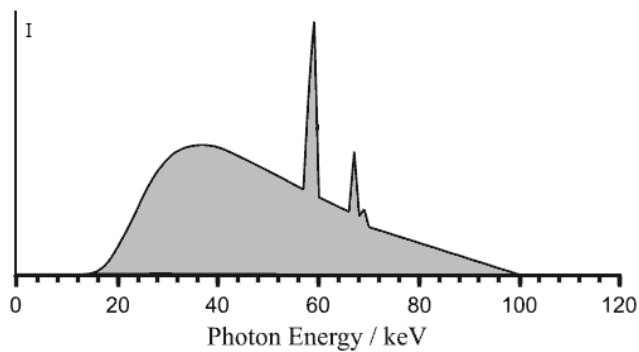


Figure 1.3: Schematic of x-ray tube spectrum.

1.1.1.2. Interaction with Matter

Through a homogeneous object, an incident radiation of wavelength λ suffers an attenuation given by the Lambert-Beer's law:

$$I(x) = I_0 e^{-\mu x} \quad (1)$$

where I_0 is the intensity of the incident radiation, and I is the beam's intensity after it traverses a material of thickness x characterized by a linear attenuation coefficient μ (cm^{-1}). If we rewrite (1) in terms of the mass attenuation coefficient μ/ρ (units cm^2/g) and the density ρ (units g/cm^3), it becomes evident that the main factor in the attenuation phenomenon is the number of atoms encountered by the x-ray beam:

$$I(x) = I_0 e^{\left(\frac{-\mu}{\rho}\right)\rho x} \quad (2)$$

Mass attenuation coefficient is a material property, independent of the physical state of the material, i.e. the number of atoms per unit volume. But it is a strong function of the effective material atomic number Z , as well as the photon energy E of the x-ray beam. In general, the mass attenuation coefficient can be described by the relationship $\mu/\rho \sim Z^m E^{-n}$, where m is equal to three or four and n is equal (approximately) to three.

Ultimately, the absorption mechanism results from the interaction between two effects: photoelectric absorption and the Compton scattering. For low x-ray energies, photoelectric absorption is predominant, instead for higher energies, the Compton scattering is more prevalent.

In strict terms, equations (1) and (2) are not enough for a complete description of the attenuation process, even if they are considered sufficient to model many situations.

1.1.2. Reconstruction from projections

Understanding the principles of tomographic reconstruction is essential to understand what CT and microCT can or cannot do, and the causes of some artifacts. Here we limit our analysis to the convolution back-projection method, which is adopted by the desktop x-ray microtomograph “SKYSCAN 1172” used for most of the experimental analysis.

1.1.2.1. Basic concepts

Equations (1) and (2) describe what can be observed after the attenuation is complete. By writing the differential form of these equations, it is possible to shift the focus on what occurs within each small thickness element dx :

$$\frac{dI(x)}{I} = \frac{-\mu}{\rho} \rho dx \quad (3)$$

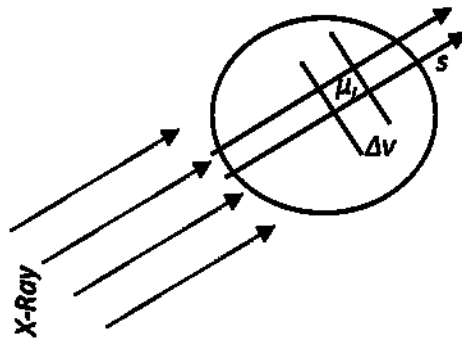


Figure 1.4: Contribution of each voxel to the total x-ray absorption along rays.

If dx represent the minimum physically realistic thickness element, then $(\mu/\rho)\rho$ is regarded as a constant and is written simply as μ . Let s be a path along an object (Figure 1.4), each voxel with attenuation coefficient μ_i contributes to the total absorption. Considering the contributions of all voxels along the propagation direction, the more general form is obtained:

$$I = I_0 e^{-\int \mu(s) ds} \quad (4)$$

where $\mu(s)$ is the linear absorption coefficient at the position s along the ray. We can rewrite the equation as

$$\int \mu(s) ds = \ln \frac{I_0}{I} = p_\theta(s) \quad (5)$$

where θ is the orientation of the parallel x-rays. The central problem of computed tomography is to assign the correct value of μ to each position in the material based only on the knowledge of the line integrals for the various orientations and positions.

As a matter of fact, locating and defining the different contributions to attenuation requires measuring I/I_0 for many different ray directions θ , and many different positions for a given θ . The sum of attenuation values at each position along the profile at θ angle, is called Radon Transform or projection, $P_\theta(s)$. The set of projections, collected at enough well-chosen directions θ , is called a sinogram.

1.1.2.2. Back-Projection

In this section, for simplicity, we describe the filtered back-projection method in parallel beam geometry. Even if most tube-based microCT systems collect data in a fan-beam or cone-beam geometry, at the limit we can describe cone beam as a parallel X-ray illumination.

As the name suggests, the filtered backprojection algorithm consists of two distinct phases: filtration, and back-projection. Let us now examine the individual "blocks" of this algorithm. To facilitate understanding, it is convenient to start from the back projection step.

Consider a rectangular object, as shown in Figure 1.5, and suppose we have performed two projections, at 0° and 90° . Each projection is a one-dimensional profile, corresponding to a row in the sinogram. Now, suppose to back projected them onto the plane. For each profile "intermediate image" (light stripes in Figure 1.5) is obtained. Superimposing the intermediate images by each profile, we obtain an approximate object reconstruction. The accuracy of the reconstruction increases with the number of back-projected angular views.

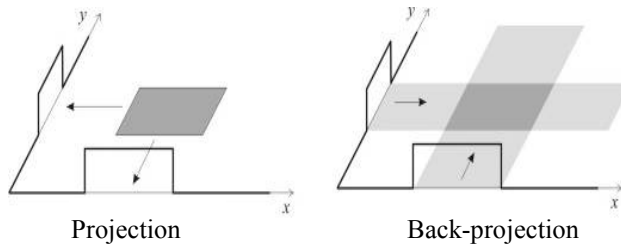


Figure 1.5: Back projection example for a square object.

Now consider the object shown in Figure 1.6, consists of two non-concentric circles at different attenuation coefficients. By performing the back projection of a growing number of angular views, an image ever more similar to the original object is obtained.

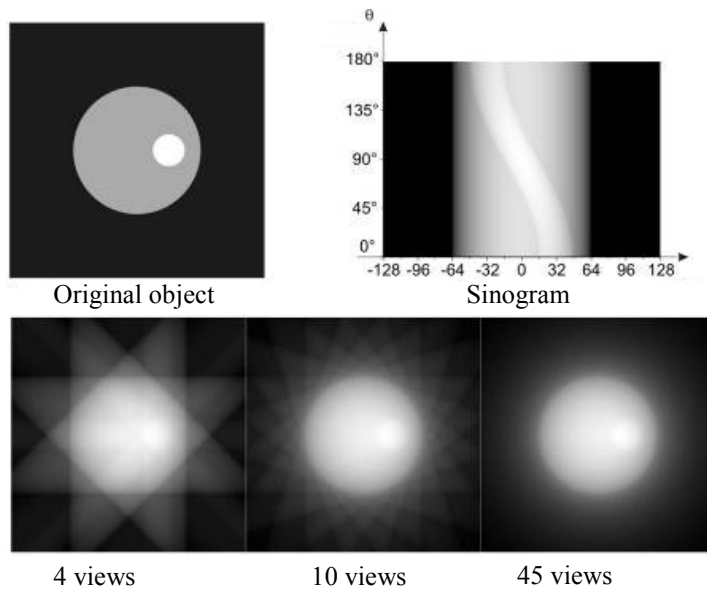


Figure 1.6: Tomographic reconstruction using backprojection.

However, the image is noticeably "blurred" because the absence of the sinogram filtration phase rather than an insufficient number of angular views.

Figure 2.6 shows another example of reconstruction, but in this case the sinogram has been filtered before the back projection. Now, the reconstructed image is better and the blur of Figure 2.5 is disappeared.

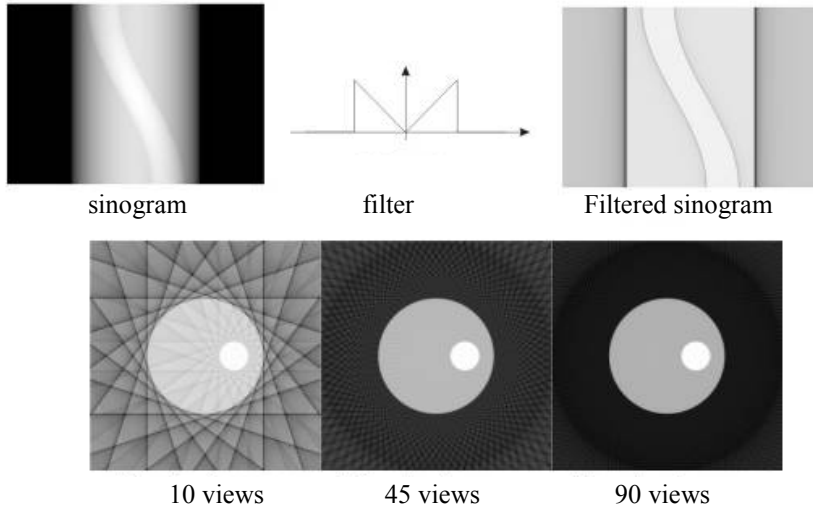


Figure 1.7: Tomographic reconstruction using filtered back-projection.

Mathematically, filtered projections are produced by convolving the filter impulse response with the projections. Although the choice of the filter function is extremely important in microCT, we will not further discuss it, here, focusing instead on a more general (brief) description of filtered back-projection.

Generally, reconstruction is carried out in polar coordinates, considering x' in a coordinate system rotated by angle θ from x (left-hand side of Figure 1.8). To understand the reconstruction it is necessary to remember that the Fourier transform of a 1D projection of the an image is equal to the radial section (slice or profile) of the 2D Fourier transform of the image at the same angle of the projection (left-hand side of Figure 1.8).

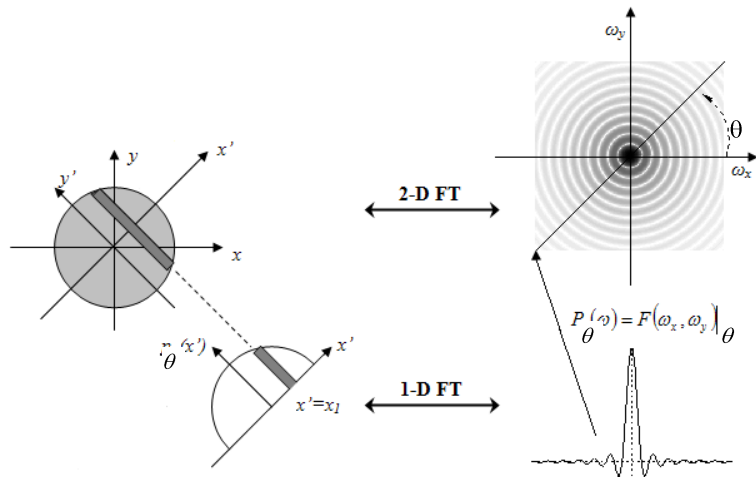


Figure 1.8: Relationship between the profile measured in the spatial domain and the corresponding representation in the frequency domain.

One obtains the map of $\mu(x,y)$, through the following steps:

- 1 Computing the Fourier transform $F_\theta(u,v)$ of measured projection P_θ for each angle θ ;
- 2 Multiplying $F_\theta(u,v)$ by the weighting function (the transform of the filter) to obtain $F'_\theta(u,v)$;
- 3 Computing the inverse Fourier transform of $F'_\theta(u,v)$ and summing over the image plane (direct space or spatial domain), which is the back-projection process.

The raw data obtained in this way by the reconstruction algorithm do not correspond yet to an image but rather to a matrix holding the absorption values in the reconstructed cross sections. After reconstruction, the raw data cross sections are converted into a grey scale image. In brief, the tomographic output is a 3D array of attenuation values converted into a stack of 2D grey-scale images.

1.2. Issues in CT imaging

In practice, real microCT systems are characterized by various non-idealities with respect to the process previously described, which greatly affect the quality of the reconstructed images.

First of all, in the application of Equations (1) and (2) it is implicit that the radiation is monochromatic; that is, the x-ray photons have a single energy level, but x-rays are polychromatic before any treatment of the beam is performed. As indicated above, attenuation coefficients depend strongly on x-ray energy (wavelength), and the presence of more than one wavelength complicates the reconstruction process as we have illustrated.

Most X-ray sources are unable to generate parallel beams, but a point source is used to produce a cone X-ray beam in the object area (Figure 1.9). In a cone beam geometry the reconstructed slices could present some distortions away from the optical axis. In order to solve these errors, a 3D cone beam reconstruction algorithm (such as Feldkamp [18]) is used to take into account the thickness of the object.

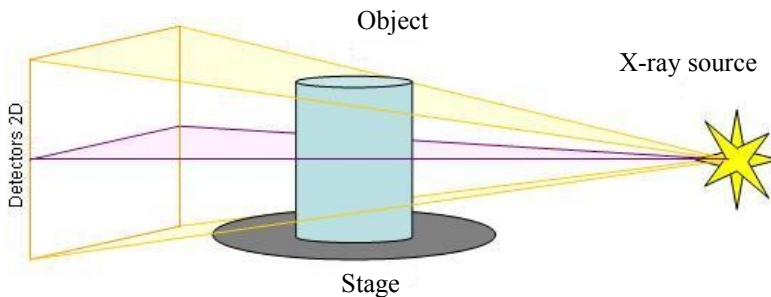


Figure 1.9: Cone beam geometry.

Then, in addition to the transmission and attenuation mechanisms, the photon scatter should be considered, which has

an unpredictable pattern since it is related to wavelength and angle of incidence.

All the previously mentioned non-idealities, as well as others, can complicate the reconstruction process and lead to errors (artifacts). Therefore, the quality of reconstruction depends on many factors, from how finely the object is sampled (i.e., the number of viewing directions and the spatial frequencies resolved in the profiles $P_{\theta}(s)$ [16]), to how accurately individual measurements of $\ln(I_o/I)$ are made despite the presence of noise and systematic errors.

In the next section we will first introduce briefly the problem of noise, treated in more detail in Chapter 3 and then will treat the effects of reconstruction artifacts.

1.2.1. Noise

The noise present in the reconstructed images depends largely on the noise present in projections. Indeed, as for many imaging devices, in microCT images noise contaminates the useful data during image acquisition. Then, the primary contributor to the total noise is the quantum noise, due to the fluctuation in x-ray detection. It leads to a random variation in the attenuation coefficients for voxels belonging to the same substance. In practice, it is possible that two voxels of the same material have different CT values.

The model commonly used to explain the origin noise in projections considers a mono-energetic x-ray source that generates quanta which are attenuated by the scanned object, and detectors that count the number of surviving quanta, with observed signal governed by Poisson statistics [19]. This model explains general observed trends of signals and noise with exposure and object attenuation.

The modern scanners, however, work in a quite different way compared with the situation we have described. An x-ray CT tube generates quanta having a continuously variable

energies spectrum, they are transmitted through objects undergoing random interactions in a manner that is strongly energy-dependent, and then the x rays interact with detectors, transforming their deposited energy into secondary optical photons. These are converted to a continuous electrical signal and integrated over time and ultimately digitally sampled. Furthermore, the measured data are often subjected to additional constraints in order to obtain artifact-free images with linear reconstruction algorithms (such as filtered back projection). In particular, some filtering are implemented, to counter the non-linearity of the acquisition process.

As can be clearly seen starting from these considerations, noise in reconstructed images poses a difficult problem, which we try to explain in more detail later.

1.2.2. Reconstruction artifacts

Artifacts might be viewed as a form of noise since they interfere with the interpretation of the CT image, but their presence is often indicated by a readily identifiable pattern. This certainly applies to the ring and the streak artifacts. The former appear as one or many "rings" within an image. This is usually due to a detector fault: detector pixels are never exactly equal in sensitivity, linearity or in spectral response, so one bad pixel will trace out a circular arc in the reconstruction (Figure 1.10).

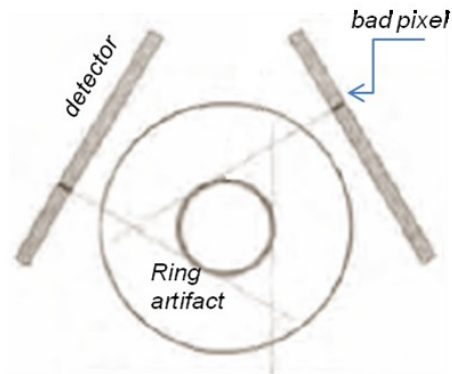


Figure 1.10: Schematic view of ring artifact.

Unfortunately they do not merely impair the appearance of an image, they also can interfere with accurate segmentation and quantification of the amount of phases present and their geometrical properties. For ring reduction, sinogram correction algorithms can be utilized, but no software method is truly effective, while shifting the camera from side to side averages out the effects.

Streak artifacts appear as bright lines which radiate away from high-absorption objects (characterized by high atomic numbers and high density) within a lower attenuation matrix. It is possible that the radiation beam is completely stopped along these radiation directions. The so-called "beam stopping" is interpreted, by the reconstruction algorithm, as the presence of objects with "infinite" attenuation coefficient. This situation is physically impossible, and the result is the appearance of the artifact in the images.

The use of polychromatic radiation produces an effect called beam hardening: when the radiation beam pass through an object, the low-energy component (*soft* component) is attenuated more than the high-energy component (*hard* component or more penetrating). As a result, the outgoing beam has an average energy greater than the incoming beam. Thus, equations (3) through (5) are no longer strictly valid as written. The hardening entity depends by the radiation line, since each

line corresponds to a different thickness traversed. As a result, the surface of the reconstructed objects appears lighter, while its interior is dark. Metal filters placed in front of the camera allow to cut the *soft* radiation and use only the high-energy part, which works in a more uniform way in the surface and inside the objects. However, by cutting out part of the X-ray radiation the number of detected photons will be reduced, which should be compensated by longer exposure time and correspondingly longer acquisition cycle.

Each pixel in a CT image represents the attenuation properties of a specific material volume; if that volume is comprised of a number of different substances, then the resulting CT value represents some average of their properties. This is named, the partial volume effect. Furthermore, because of the inherent resolution limitation of x-ray CT, all material boundaries are blurred to some extent, and thus the material in any one voxel can affect CT values of surrounding voxels.

In current generations of microCT systems the only required specimen motion is rotation and accurate reconstruction requires that the center of rotation has to be defined very precisely. Poor centering causes arc artifacts. An automated centering procedure gives a sinogram which is better centered on the rotation axis by determining the center-of-gravity of each row in the sinogram. The sinogram is then shifted left or right so that the rotation axis is exactly on the center column of the sinogram array.

Due to the many error sources, it is best to collect the highest quality data possible, even if software can ameliorate the effects of instrumental non idealities and from less-than-optimum sampling dictated by experimental requirements.

Chapter 2

Morphology approach on image analysis for porous media

The X-ray computed micro-tomography allows non-destructive three-dimensional analysis of the porous media interior. The analyzed sample acts as a filter that attenuates the X-ray energy in proportion to the density and the atomic number of the material. The set of reconstructed images is a three-dimensional sample density map and therefore provides valuable information on the composition of the object under examination.

While micro-CT datasets can be used directly for imaging and qualitative analyses of porous media, a continuing challenge is the development of quantitative tools/algorithms able to characterize the porous media internal structure. Commercial image-analysis packages contain a number of computational tools that provide good starting points. However, for the quantitative analysis of the porous media internal architecture, most suitable and specific tools are required than those available from standard commercial software. In this chapter, we propose 3D image analysis procedures in order to supply a quantitative characterization of the porous media inner structure. In particular, we present a new approach to the analysis of 3D porous media microstructure based on mathematical morphology theory.

Mathematical Morphology (MM) is a form of nonlinear image processing and analysis, initially developed by Serra [6]

and Matheron [20], used for studying the geometric structure of images. The MM consists into a powerful and flexible set of methods for extracting different sorts of information, and its scope is as wide as image processing itself. The basic concept, derived from stereology, is to compare an image with a reference object, called structuring element (SE), and to quantify the way in which the SE is contained or not into the image. Of course, this result depends on SE size and shape, and therefore on the user selection.

Nowadays morphological image processing is a standard part of the imaging scientist's toolbox and is applied daily to a wide range of industrial applications, such as biomedical imaging, document processing, pattern recognition, remote sensing, microscopy, robot vision and others. Because the MM theory can be considered as a universal language for image processing, regardless of the application, its only limitations are given by the ability to design effective algorithms and efficient computational implementation.

In this chapter, we present only a few fundamental notions from mathematical morphology, which we will use to formulate our proposal. We refer the interested reader to the textbooks of Serra [6] and Matheron [20] which provide a comprehensive introductions to mathematical morphology. We skip over the non-trivial steps of filtering (see Chapter 3) and segmenting (see for example [21]) a 3D image, assuming as a starting point a high-quality binary² data set for the material of interest.

² The binary value denotes whether a voxel belong to the void or solid phase.

2.1. Porous media image analysis objectives

Initially, we have defined a porous medium as a solid structure with interconnected voids. Indeed, porous media contain regions of void, which form the pore space. But more generally, both the voids and solid can be considered as different phases which compose a porous medium.

The spatial distribution and relative amounts of different phases are responsible to a great extent of the macroscopic properties of the material. Therefore, to understand the role, distribution, connectivity, and in general, the morphology of each phases is crucial for many applicative fields interested to porous media. This is certainly true for the two specific applications, geo-science and biomedical, considered in the following of this Chapter.

2.1.1. Geo-Sciences applications

The soil is called the “Earth’s thin skin” [22] because it works like a delicate interface between different systems: hydrosphere, biosphere, atmosphere and lithosphere. It is a dynamic system in which complex processes occur. Furthermore, soil provides diversified services, including water supply and food production, valued over 33T\$ [23].

Nearly all functions of soil depend to some extent on its complex structure as a porous medium. Indeed, soil structure determines the ecosystem functionality by regulating the distribution of water, oxygen and nutrients. Therefore, by controlling water transfers, morphology and connectivity of porous structures affect also physical, chemical and biological processes which rely on the availability of water and gases flowing through soil pores.

Although the importance of soil structure is universally recognized, carrying out a quantitative analysis of its properties is not a trivial problem. First of all, the soil is an opaque medium, therefore, it can be analyzed by means of simple but invasive methods or else by resorting to advanced technologies which return non-invasive measurements. Soil structure can be analyzed at different scales, from the pores between individual particles, up to large macropores that embrace the whole soil profile. Regardless of the scales, they have a wide variety of complex shapes, so simple indicators do not return relevant information. X-ray computed tomography, though, allows to investigate the three dimensional structure of materials at a fine resolution, and this offers the possibility to explain and predict soil characteristics.

2.1.1.1. State of art for feature extraction

With the development of digital image processing there has been an expansion in the quantitative analysis of soil structure, starting with two-dimensional images of thin sections or polished surfaces of soil blocks, which can be obtained from undisturbed samples impregnated with resin [11] [24] [25]. Today there are various tomographic techniques (see Chapter 1) available for a three-dimensional non-invasive visualization of structural properties. These include MRI and X-ray tomography using polychromatic X-rays (as in medical applications) but also monochromatic synchrotron radiation, to gain spatial resolution down to microns. Starting from images generated by these techniques, the structural features of interest are extracted, such as porosity, pore diameter, perimeter and area, equivalent cylindrical diameter, tortuosity³, hydraulic radius in three-dimensions (pore volume/wall area), numerical density of

³ The path tortuosity is defined as the shortest path between two volume extremes, divided by the Euclidean distance between the two points

networks and connectivity. The next logical goal is the quantitative characterization of the pore space in order to link structural properties to soil functions, including water flow and solute transport processes. In addition, by connecting the soil structure to its physical properties, one can understand the impact of the structure formation processes, useful in soil management, soil mechanics and soil hydrology.

Typically a statistical description of structural features is used, by which the structural complexity is reduced to a limited but meaningful set of numbers that ideally can be related to physical properties. Among the main methods proposed in the literature [26] [27] [28], the most widely used to derive soil properties is the pore-throats analysis, mainly because the theory behind this approach has been in a source code, the 3DMA-Rock Primer [2], available to all interested researchers.

PORE-THROATS ANALYSIS

The procedure consists of two steps: the medial axis construction and the throats extraction.

Once the stack of images are segmented, the medial axis is constructed by using a burning algorithm developed by Lee et al. [29] and modified by Lindquist et al. [28]. The medial axis (ma) of an object is the skeleton of the void space of an image and it runs along the voids geometrical middle [28] [30]. The burning algorithm is applied as follows (Figure 2.1): each voxel in the solid phase is labeled with integer 0, and voxels in the void space are initially unlabeled.

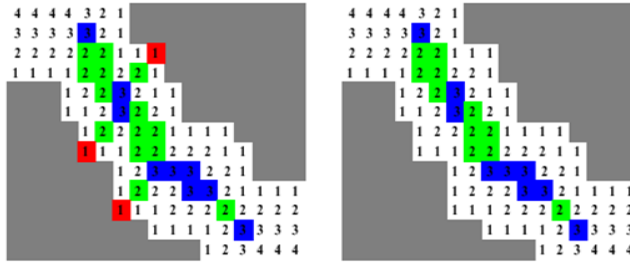


Figure 2.1: Two-dimensional illustration of medial axis determination

The algorithm begins with $n=0$ and labeling with $n=n+1$ all the voxels adjacent⁴ to those belonging to the solid phase. At this point the algorithm restarts from voxels not labeled and continues at a rate of one layer per iteration until all voxels in the pore space are labeled. Then, the medial axis is determined by the voxels where different solid-pore boundaries intersect.

The result of this burning algorithm is a set of medial axis voxels, each with a unique burn number k , identified by a colour code in Figure 2.1, depending on its distance from the surface. Pores are then identified as the volumes around voxels that have local maximum distance from the surface, and similarly, the throats are defined by voxels having local minimum distance measure.

At this point, once the pores have been identified by the throats, they can be used to calculate the bulk porosity of the sample. Moreover, the medial axis stores some information such as spatial location and the burn number of each voxel. They can be used to learn the pores spatial position in the sample and their geometrical features, such as specific surface area⁵ and pore distributions of disconnected volumes

⁴ There are several methods to define the 3D neighborhood of a voxel, see §2.3.2 for further details.

⁵ Specific surface area (SSA) represents a measure of the interstitial surface area of the void-solid phase per bulk volume, and it is calculated by summing

The major shortcoming of this approach is the problem of extracting a pore–throat network that is both geometrically consistent and intuitively correct. Not always in fact, the pore definition, proposed by this approach, coincides with what one subjectively might think. For example, analyzing the structure represented in Figure 2.2, in all three cases, (a), (b) and (c), the a-b segment corresponds to the throat definition and all three examples would be considered as showing two pores. However, it could be also argued that (a) represents the case of a single pore while (c) represents two pores.

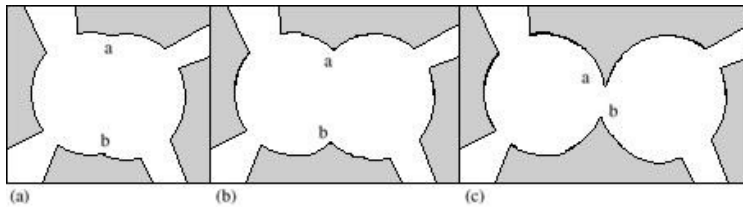


Figure 2.2: An illustration of the difficulty in determining single pore bodies.

Indeed, this automatic procedure of medial axis construction could produce some incorrect results. If throat construction procedure fails in some conditions, pore objects can be identified in unexpected ways, leading to wrong results. Indeed, pore-throat analysis, for extraction of pore networks, has too many subjectivity problems, such as of type related to Figure 2.2, that lead to inconsistencies in the resulting pore network.

2.1.2. Biomedical applications

Bone is a specialized form of connective tissue and the main component of our skeletal system [31].

the areas of all void-solid material voxel faces, and dividing this area by the total image volume.

Despite its robustness, the bone is light, thanks its structural organization. It is characterized by the presence of compact bone tissue, usually localized in the outer part of bones, consisting in a solid material, and spongy bone, located inside and composed by a multitude of support fiber like boards, called trabeculae. These delimit the boundaries of the cavity that host the bone marrow, see Figure 2.3. This extraordinary internal organization gives the maximum strength properties associated with low weight, and it is one of the most important attributes of the bone tissue, which makes it suitable to support the body and for the protection of the viscera, but also to the movement.

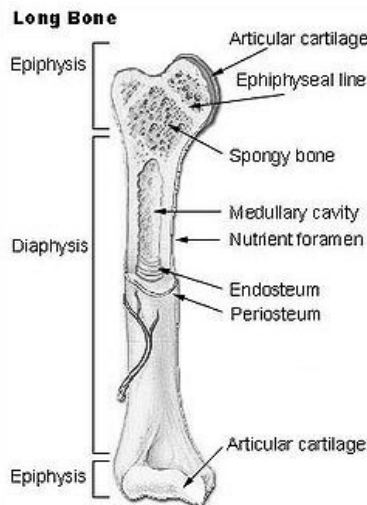


Figure 2.3: Illustration of a long bone showing the diaphysis, epiphyses, medullary cavity, cortical and trabecular bone.

The bone is not static but is a living tissue, constantly renovated and remodeled in order to perform its mechanical functions and for calcium concentration regulation process in plasma.

In recent years, many studies [32] [33] [34] on tissue morphology characterization and on cancellous (or trabecular) bone architecture have been conducted, particularly to learn the

important relation between morphometric parameters and mechanical performance. Interest in these issues comes from the wide spread of diseases, such as osteoporosis, which are associated with alterations in bone tissue structure and composition, with concomitant changes in skeleton functionality and mechanical characteristics (brittle bones, high fractures risk).

Wolff [35] established the hypothesis that “Every change in the form and function of bones, or of their function alone, is followed by certain definite changes in their internal architecture and equally definite secondary alteration in their external conformation, in accordance with mathematical laws”. Although the relationship with possible mathematical laws has been questioned, it is not doubted that mechanical charges affect the internal organization of bone. For diagnostic purposes, it is therefore of great interest the development of methodologies for accurate assessments of the bone tissue histo-morphometric parameters.

For years, stereology applied to histological sections has been the "gold standard" for the evaluation of bone tissue microarchitecture and, in particular, of the trabeculae structural organization. It consists of extracting bone samples and analyze histological sections (two dimensional) using conventional histomorphometry. Thanks to the progress achieved by high-resolution imaging systems, it is now possible to assess directly the three-dimensional microarchitecture of the bone samples in vitro.

2.1.2.1. State of art for feature extraction

Morphological parameters reflect trabecular size and spacing, as well as porosity. The earliest parameters were proposed by Parfitt [36] and were originally designed for calculation from 2-D images acquired after the processing of bone tissue samples. Many variables used for conventional histomorphometry can be used with high resolution images, and they have been discussed

in detail in two reviews published in Joint Bone Spine [37] [38]. Here we only summarized some of them:

- Bone Volume (Bone Volume/ Tissue Volume [BV/TV]): This 3-D parameter relates bone volume to total tissue volume. The number of voxels with bone is then divided by the total number of voxels.
- Bone Surface (Bone Surface/Bone Volume [BS/BV]). This 3-D parameter relates the bone surface to total bone volume. It increases with a decrease in the number of trabeculae.
- Number of trabeculae ([Tb.N]). This 2-D parameter can be calculated by using the Mean Intercept Length (MIL) method developed by Whitehouse [39]. A grid of parallel lines is superimposed on the image. A ratio is obtained between the intersection points of the lines and the bone-marrow interface of the trabeculae, in relation to the total length of the grid-lines. This method can also be used to obtain trabecular separation (Tb.Sp) and trabecular thickness (Tb.Th) parameters, but it is not valid for 3-D assessment.

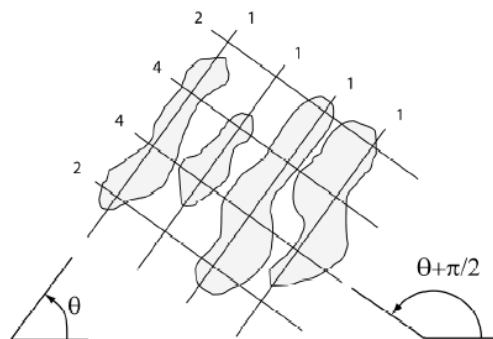


Figure 2.4: Mean intercept length. The number of bone-marrow interfaces is counted along the parallel lines through the specimen for different angles θ .

- Index of the structure of the model (Structure Model Index [SMI]). This variable indicates the prevalence of

the rod-like or plate-like structures of the trabecular structure. It is quantified from level 0 (plate-like structure) to level 3 (rod-like structure) [40]. Osteoporosis is characterized by results that range from plate-like to rod-like structures of trabeculae.

- Degree of Anisotropy (DA). The concept of isotropy refers to the completely regular or irregular spatial orientation of a structure. Thus, bone that usually presents completely disoriented structures (trabeculae) combined with oriented structures (depending on the load) is considered anisotropic material [41]. The DA can be obtained from a 3-D image, as the ratio of the maximum to minimum radius of an ellipsoid created by the MIL method using a grid on all dimensions of the volume of interest. The DA increases with a decrease in the biomechanical resistance of bone and is reduced by the trabecular orientation caused by loads (isotropic orientation). It can also be obtained using the Volume Orientation (VO) method described by Odgaard [41].
- Number of Havers Canals/Cortical Bone Area ($N.Ca/Ar$). This variable is used to assess the porosity of cortical bone alone. A resolution of at least 20 μm is required for its assessment.

2.2. The morphological approach

In this thesis, we propose a new approach to the analysis of porous media microstructure, based on the methods of mathematical morphology. Although mathematical morphology theory is well established by now, and widely known, we introduce here some basic concepts that are needed as foundations for the remaining sections of this chapter.

2.2.1. Some basic concepts

The language of Mathematical Morphology is set theory. Sets represent objects in an binary image⁶. The discrete binary image, A , is defined as a finite subset of Euclidean 2-D or 3D space, that can have the values 0 and 1. Morphological transformations are visualized as working with two images, namely the image being processed, A , and the structuring element, B , that possesses certain characteristic information such as shape, size, orientation, and origin. The structuring element (SE) is usually represented as an array. For easy viewing, we use the convention to set the background values to 1 and foreground values to 0. The Figure 2.5 shows some examples of commonly used 2D structuring elements.

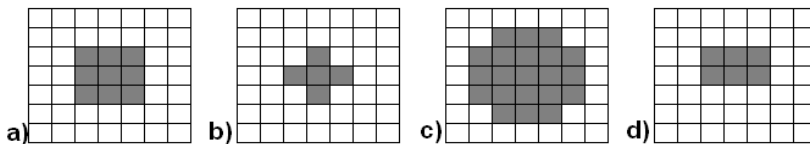


Figure 2.5: Some 2D structuring elements, a) square, b) cross, c) circle, d) line

The image A can be decomposed by probing it with various structuring elements to unravel certain complex features of its topological nature.

A morphological operation transforms A to a new image by a structuring element B . The four basic morphological operators are *erosion*, *dilation*, *opening* and *closing*, that are defined with respect to the structuring element B .

⁶ Although the definitions are very general, for ease of exposition, the examples refer mainly to two-dimensional black-and-white images. However, the concepts are readily extended to 3D and gray-scale images.

2.2.1.1. Erosion

The operation of *erosion* represents the probing of an image to see where some primitive shape fits inside the image, and all of mathematical morphology depends on this notation. It is defined as follows:

$$A \ominus B = \{x | B_x \subset A\} \quad (6)$$

where A is the image to be processed, B is the SE and B_x is the translation of B with respect to a vector x . In other words, the result of the *erosion* of image A by structuring element B is the set of points x such that B_x is completely contained in A . In Figure 2.6 we show a 2D example of *erosion* operator with a 2x1 structuring element, while Figure 2.7 shows an example of *erosion* with a circular structuring element.

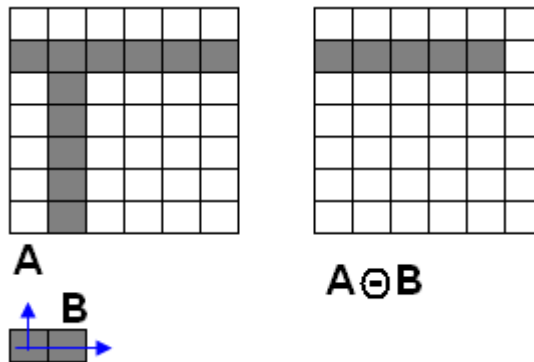


Figure 2.6: *Erosion* of A by structuring element B .

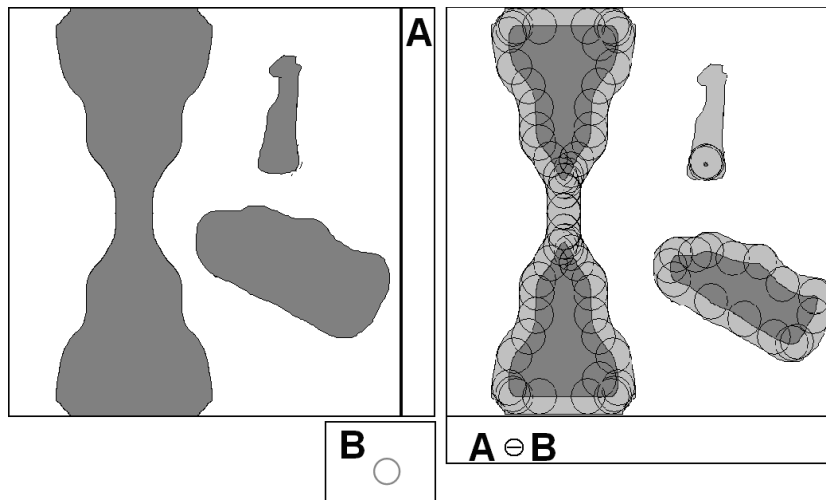


Figure 2.7: *Erosion of A by circular structuring element B.*

2.2.1.2. Dilation

Dilation is the dual operator of *erosion* and is defined as follows:

$$A \oplus B = \{x | B_x^r \cap A \neq \emptyset\} \quad (7)$$

where A is the image to be processed, B is the SE and B^r means the reflection of B . In Figure 2.8 we show a 2D example of *dilation* operator with a 2×1 line structuring element.

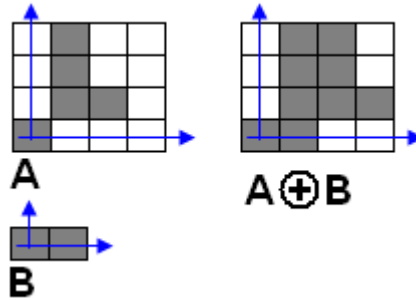


Figure 2.8: *Dilation of A by rectangular structuring element B.*

The *dilation* of the image A , using the structuring element B , can also be seen as the locus of points covered by B when the center of B moves on A ; or otherwise exploiting the duality of the *erosion* and *dilation* operators, the result equivalent to applying the *erosion* operator to the complement of the image A (see Figure 2.9).

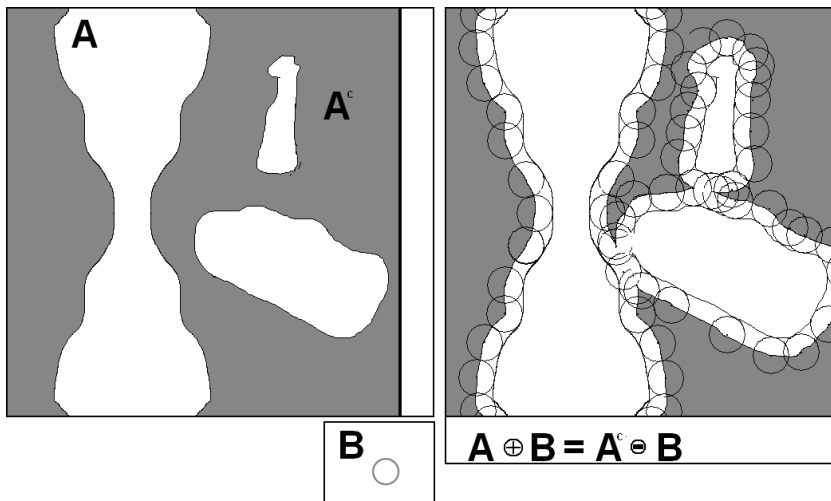


Figure 2.9: *Dilation of A by circular structuring element B.*

Besides the two primary operators of *erosion* and *dilation*, there are two secondary operations that play key roles in morphological image processing, *opening* and *closing*. We

focus mostly on *opening*, because is the key operator of our algorithms.

2.2.1.3. *Opening*

The operation of *opening* is the application of an *erosion* followed by *dilation* and is defined as follows:

$$A \circ B = (A \ominus B) \oplus B \quad (8)$$

Although *opening* is defined in terms of *erosion* and *dilation*, it possesses a more geometric formulation in terms of structuring element fits, which is the foundation for its relevance. In fact, the *opening* operator removes regions that are unable to fully contain the structuring element, while those that contain it remain unchanged (see Figure 2.10).

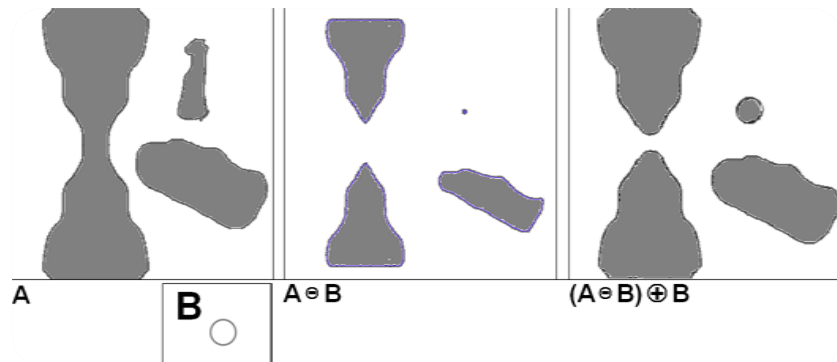


Figure 2.10: *Opening* of *A* by circular structuring element *B*.

2.2.2. The “Successive Openings” algorithm

The "Successive Opening" morphological algorithm, used here to characterize porous media, consists in the repeated application of the *opening* operator using spherical structuring elements of increasing diameter. By applying the *opening* operator to the original digital representation of the considered phase space we remove those parts of the structure which are “smaller” than the structuring element. In the following we will call these parts as size classes.

After the first iteration, object features whose smallest dimension is less than the SE, i.e. that could fit within the volume of the SE, are eliminated. The structuring template size increases from iteration to iteration, and after every step the part of the structure characterized by a dimension less or equal to the SE diameter is intercepted and removed. After n iterations, only object features larger than the n -th SE’s diameter remain. Therefore, Successive Openings with spheres of increasing radius gradually eliminate larger and larger objects.

The Figure 2.11 shows the algorithm flowchart, where we call O_n the result of *opening* operator to a binary image with a spherical SE of radius n .

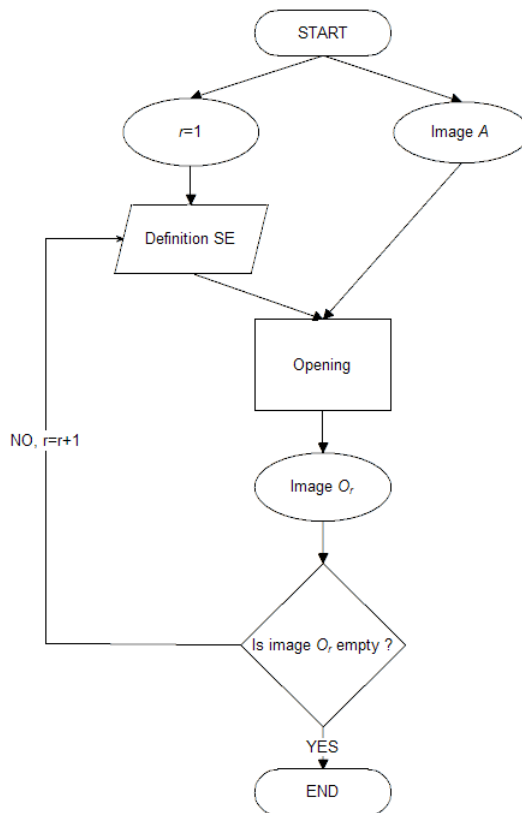


Figure 2.11: Algorithm flowchart

As an example, we show the algorithm effect on a 2D test image, using an incomplete subset of 2D spherical SEs family, characterized by increasing diameters. Figure 2.12 shows SEs for different value of radius r (in pixels). The color code is used only for didactic scope.

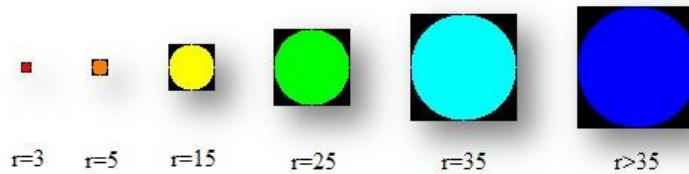


Figure 2.12: Incomplete SE subset with increasing diameters.

Figure 2.13 shows (on the right) the effect of *opening* with circular SE of radius $r=3$, and (on the left) the intercepted portion of the object, shown in red.

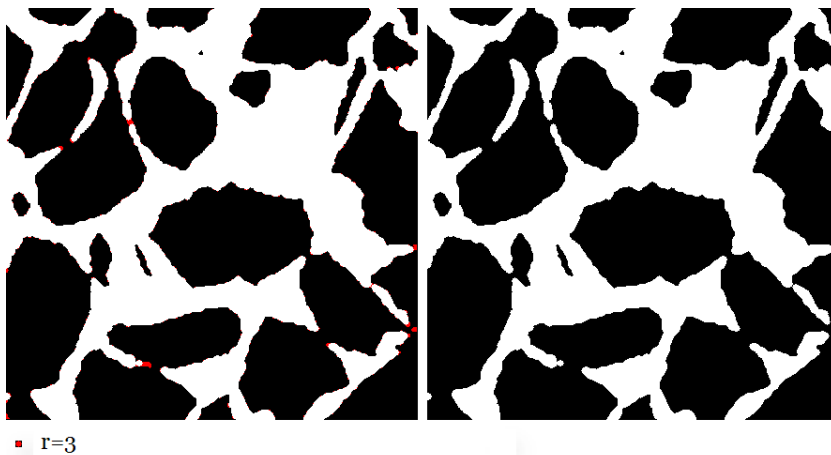


Figure 2.13: Effect of *Opening* with circular SE of radius $r=3$.

By increasing the SE radius to 5, the orange size class is eliminated and we obtain the result depicted in Figure 2.14.

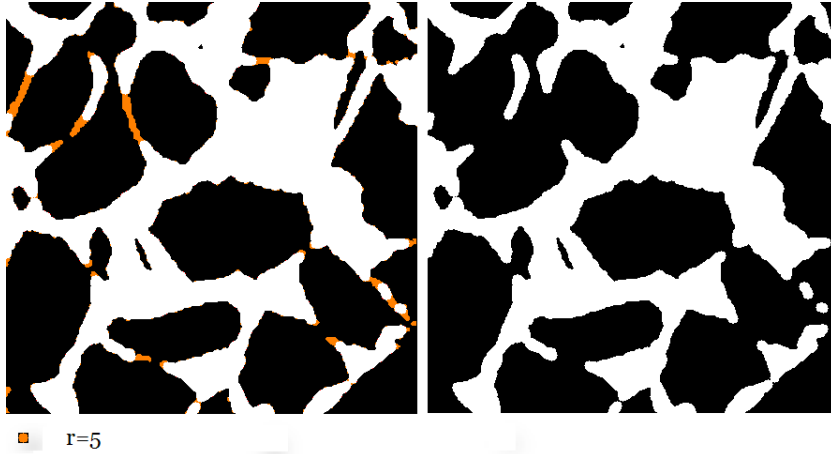
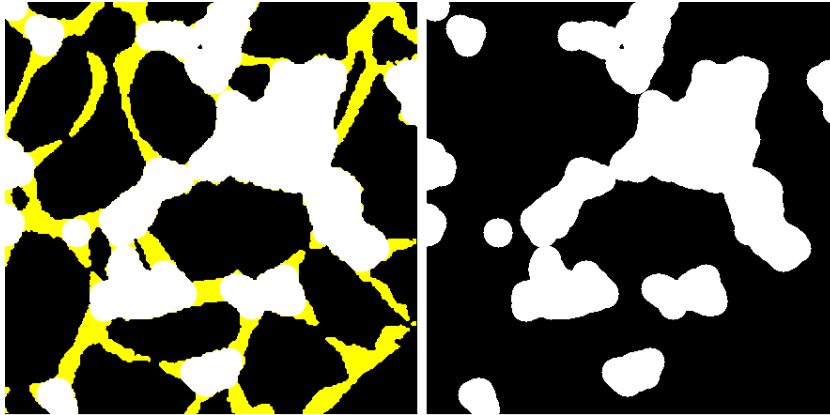


Figure 2.14: Effect of *Opening* with circular SE of radius $r=5$.

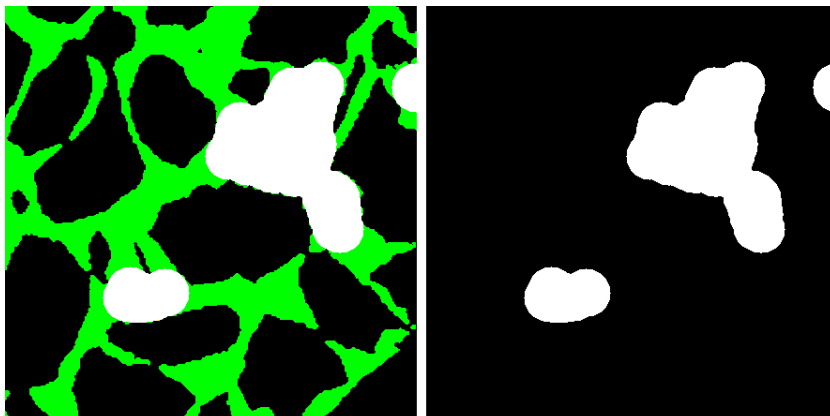
With increasing SE diameter, larger and larger portions of the objects are intercepted and, at the same time, the foreground is reduced gradually, assuming a peculiar shape. The resulting effect is that of a series of circles (spheres) of increasing diameter, which run inside the whole image and fill the objects having size minor or equal to the current diameter.

Then, in this case, after having intercepted the size classes in red (Figure 2.13) and orange (Figure 2.14), the *opening* operator, with SE of radius 15, 25 and 35, eliminates respectively, classes in yellow, green and cyan (Figure 2.15, Figure 2.16 and Figure 2.17). When the SE radius reaches the maximum size of the objects represented, all size classes are intercepted and eliminated.



● $r=15$

Figure 2.15: Effect of *Opening* with circular SE of radius $r=15$.



● $r=25$

Figure 2.16: Effect of *Opening* with circular SE of radius $r=25$.



Figure 2.17: Effect of *Opening* with circular SE of radius $r=35$.

2.2.2.1. Shape of structuring element

The results obtained from mathematical morphological filtering depend strongly on the SE's shape.

In the study of porous media, given the very high anisotropy of the objects in question, the best choice is to use a spherical shape SE. In fact, the objects of interest are characterized by a very irregular structure, so that it is already difficult to define the section diameter, which varies within the same object and depending on the position. To overcome this ambiguity, it is worth considering as a reference dimensional parameter, the minimum distance between the object walls. So it is clear why the sphere is used as SE, since it intercepts points equidistant from its center and therefore it is best suited to the identification of the minimum distance between the walls, no matter their orientation. It is therefore necessary a SE that works independently of the particular orientation considered. The aim is to perform an isotropic filtering and the only solution is to use a (approximating) spherical SE. In particular a spherical SE is

calculated according to the Euclidean distance of voxels from the centre of the SE.

Unfortunately, using this kind of SEs, morphological filters have the great disadvantage of requiring long computing times and large computer memory since, as SEs grow bigger, the number of voxels to check against each voxel in an image increases proportionally to the third power of the radius [42]. In next section we propose an alternative version to “successive openings” algorithm, that is able to obtain very close results, but in much lower times.

2.2.3. A fast implementation

Although particularly suited to shape and size measurements in 3D, quite surprisingly mathematical morphology has not been much used in studies using X-ray micro-CT to unravel the three-dimensional complexity of porous media, probably for the computer memory requirements associated with handling increasingly large approximated spheres.

It is worth underlining that two-dimensional versions of morphological filters have already been used in soil science by Horgan (1998) [43], he replaces a radius- n *opening* operator with n cycles of *opening* with unitary radius. Unfortunately, the two operations are not equivalent, unless certain conditions are met.

2.2.3.1. Simplified *opening*

An interesting feature of the *erosion* and *dilation* operator is that they can be broken down. In other words, if transformations with large structuring elements are required, which would be computationally demanding to implement directly, one can divide this transform in several transformations with smaller structuring elements. For example, an *erosion* with a sphere of

radius r , repeated n times, is equivalent to an *erosion* with a sphere of radius nr .

On the contrary, this property does not apply for *opening* and *closing* operators because of their idempotence propriety:

$$(A \circ B) \circ B = A \circ B \quad (9)$$

Then assuming that B_1 is a unit-radius structuring element and B_k is a spherical structuring element of radius k :

$$A \circ B_k \neq \underbrace{(\dots ((A \circ B_1) \circ B_1) \dots \circ B_1)}_{k\text{-times}} = (A \circ B_1) \quad (10)$$

For this reason, the *opening* task is often broken up in its components, *erosion* and *dilation* and a simplified version is implemented:

$$\begin{aligned} A \circ B_k &\neq \underbrace{(\dots ((A \ominus B_1) \ominus B_1) \dots \ominus B_1)}_{k\text{-times}} \underbrace{\oplus B_1 \oplus B_1 \dots \oplus B_1}_{k\text{-times}} \\ &= (A \circ B_1) \end{aligned} \quad (11)$$

Furthermore, a property of *erosion* operator is that:

$$A \ominus (B \oplus C) = (A \ominus B) \ominus C \quad (12)$$

Which implies:

$$\begin{aligned} A \circ B_k &\approx \left(A \ominus \left(\underbrace{B_1 \oplus B_1 \dots \oplus B_1}_{k\text{-times}} \right) \right) \\ &\quad \oplus \left(\underbrace{B_1 \oplus B_1 \dots \oplus B_1}_{k\text{-times}} \right) \end{aligned} \quad (13)$$

where the sign of equality holds only assuming that:

$$B_k = \left(\underbrace{B_1 \oplus B_1 \dots \oplus B_1}_{k\text{-times}} \right) \quad (14)$$

A SE as B_k is called homothetic convex structuring element.

Unfortunately the Euclidean sphere does not satisfy the property (14) in the discrete grid, so the equivalency in (13) is only approximate.

Nevertheless, one could decide to use a SEs family that satisfies the condition (14), such as octagons. So, an *opening* of size n is the result of n elementary *erosion* and n elementary *dilation*, with SE of radius $r=1$. In this case, the computing time depends on the number of cycles, but not on the SE radius. Unlike spheres, however, octagons are not isotropic and this means that increasing cycle numbers, the “successive openings” algorithm result is far from the original one.

2.2.3.2. Our proposal

Spherical SE corresponds closely to the idea of the hydraulic pore diameter, according to the capillary rise equation, and we do not want to renounce this feature. Regrettably, as we have seen, the algorithms that use *opening* operator require processing time quite high and big computer memory.

To overcome this limitation we propose an alternative algorithm to “successive openings”. Starting from what is suggested by Meyer [42] about MM in three dimensions, we define a method that, using the distance transform, guarantees the same effects of “successive openings” algorithm, but with greater execution speed. The basic idea is to use the properties of the distance transform and exploit the built-in nature of *dilation* operator.

The *opening* is a derivate operator using basic functions like *erosion* and *dilation* which are implemented more

efficiently. Using only the built-in operators, we are able to significantly reduce processing time.

DISTANCE TRANSFORM

For a given set A , we define the distance function or distance transform $DT(A)$ in the following manner: for any point x in A ,

$$DT(A)(x) = \min\{d(x, y), y \in A^c\} \quad (15)$$

That is, the distance from x to the complement of A . The concepts of distance transform and *erosion* are related, in fact, if we define a sphere of radius r as a set of points within r of the origin:

$$B_r = \{d(u, (0,0,0)) \leq r\} \quad (16)$$

The distance transform of A stores the erosions of A by a family of spheres: the pixels that are at a distance below or equal to r from the background are the pixels removed by the *erosion* of A by the sphere of radius r . This property is useful for geometric interpretation of the distance transform and the *erosion* by spheres; but it is also useful in the design of efficient algorithms, both for *erosion* by spheres, or to compute the distance transform [44]. Specifically:

$$A \ominus B_r = X_{r+1}(DT(A)) \quad (17)$$

where $X_k(f) = \{x: f(x) \geq k\}$ is the threshold set of f at level k . Indeed, through distance transform algorithms optimized, one can get the distances map efficiently.

THE “SUCCESSIVE *OPENING*” ALTERNATIVE ALGORITHM

The distance transform is a powerful and elegant algorithm, which somehow integrates the information we need. At this point, one only needs to find a way to extract them.

Reminding once again that the *opening* is defined by an *erosion* followed by *dilation*, the first step is to consider that the *erosion* part of the *opening* operator is contained in the distance map, so it remains to define the *dilation* phase.

The ultimate goal is to get the opened⁷ O_n image of order n , for all n . O_n is an image in which there are only objects with a size greater than n , the size classes of a lower order are therefore eliminated. We can, however, revise this result as the presence of last $M-n$ size classes, rather than the absence of the first n classes, if M is the maximum objects size in the image A . In other words, the basic idea is to get the opened image of order n , by adding size classes at greater distance, instead of eliminating lower distance size classes. This is achieved by dilating points, at a distance greater than n , identified with the distance transform. We formalize this idea into an algorithm in two steps:

1. calculate the distance function $DT(A)$;
2. for $i=1$ to M , define G_i as a particular function of $DT(A)$ where only the voxels with a value equal to i are dilated by a spherical SE of radius $r=i$.

The opened image of order n is obtained adding G_i sets, with decreasing i from M to $n+1$. Figure 2.11 shows the “successive openings” alternative algorithm flowchart.

⁷ We call opened image the result of *opening* operator .

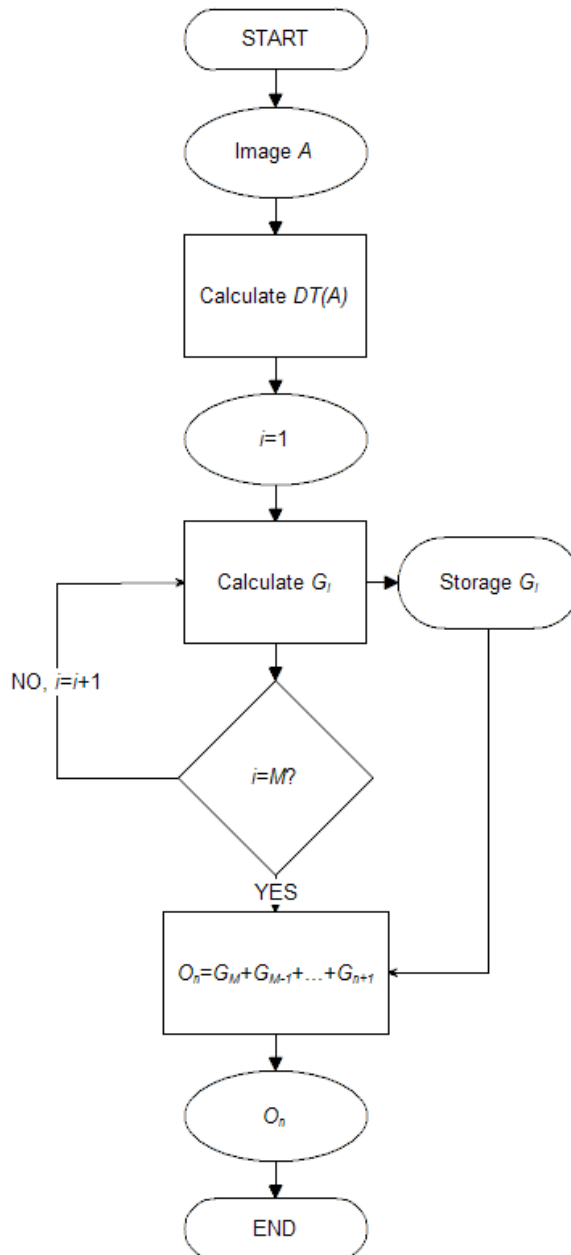


Figure 2.18: Alternative algorithm flowchart.

In Figure 2.19, we show a 2D example of the result obtained with the proposed algorithm. On the left, we report the opened image of order 11, O_{11} , obtained by the “successive openings” algorithm with a circular SE. Figure 2.19 (b), instead, is got by adding all the G_i (shaded) functions, for every $i > 11$.

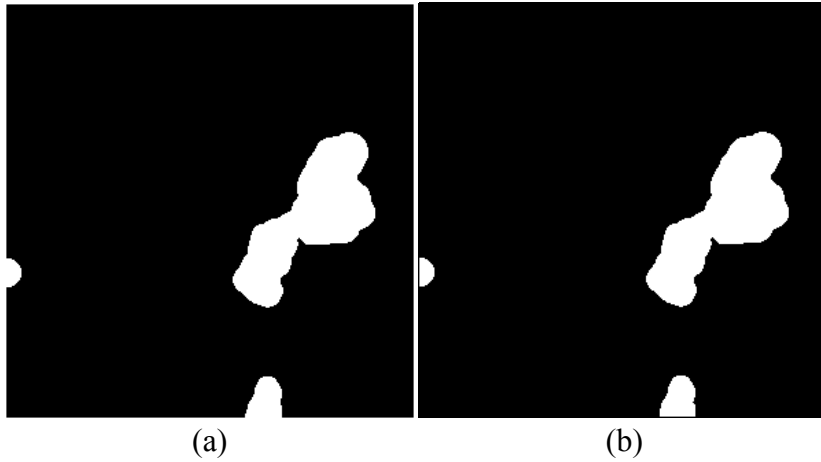


Figure 2.19: (a) O_{11} image; (b) sum of G_i functions.

2.3. Quantification of features

Once defined the methodology and then the analysis algorithm, we use it to propose several indicators. Remember that the ultimate goal is to provide, to the final user, some statistic data that are easy to understand, but at the same time, that are strongly correlated with the characteristics and structure of porous media considered. For this purpose, we define the following indicators:

- Dimensional curves, that explain how the object size is distributed in the volume of interest (VOI) as a function of the SE diameter. For application on

porous phase, we call this curve Pore Size Distribution (PoSD); for applications to the solid phase, instead, we call this curve Trabecular Size Distribution (TrSD).

- The percolation curve; we investigate the existence of paths and connections between any two extremes of the volume, and evaluate the characteristics of these connections.
- Effective porosity; we extract from the whole porous phase volume, the fraction that is really interested by fluid passage.

These indicators, which we describe next, allow together to quantitatively characterize the internal structure of a porous medium.

2.3.1. Dimensional curve

The dimensional curve concept is not entirely new in the study of porous media. Traditionally, to study the solid phase of a porous medium, the granulometry [20] is employed, which seeks to capture the result of a sieve analysis for granular media. If an image is considered as a collection of grains, then whether an individual grain will pass through a sieve depends on its size and shape, relative to the mesh of the sieve. By increasing the mesh size, while keeping the basic shape, more and more of the image will pass through, the eventual result being that no more grains remain. The number of grains (or their volume) that pass through each one of the mesh size considered, represents a point on the granulometry curve.

Similarly, let us consider the class of operator O_i defined by:

$$O_i(A) = A \circ B_i \quad (18)$$

with A a binary image and B_i spherical SE of radius $i > 0$. If $\Omega(i)$ is the volume removed by *opening* by B_i , then

$$\Omega(i) = v[A] - v[(A \circ B_i)] \quad (19)$$

where v denotes volume, $\Omega(0) = 0$ and $\Omega(i)$ is an increasing function of i . Under the assumption that A has finite extent (which is certainly reasonable for image processing), $\Omega(i) = v[A]$ for sufficiently large i . $\Omega(i)$ is called a discrete size distribution.

A normalized size distribution is defined by

$$\Phi(i) = \frac{\Omega(i)}{\Omega(\infty)} = \frac{\Omega(i)}{v[A]} \quad (20)$$

$\Phi(i)$ increases from 0 to 1 and can be seen as the cumulative distribution function of a discrete random variable. Thus, its discrete derivative

$$d\Phi(i) = \Phi(i + 1) - \Phi(i) \quad (21)$$

can be seen as the corresponding probability distribution function (probability mass function).

Plotting $d\Phi(i)$ ⁸ for i going from 1 to M , the maximum object dimension, we obtain the dimensional curve which gives the fraction of the phase, in this case as percentage, corresponding to each value of the SE radius. As an example, in

⁸ In granulometry, $d\Phi(i)$ is known as the pattern spectrum of the image.

Figure 2.20 we show the dimensional curve for the 2D binary image used in §2.2.2.

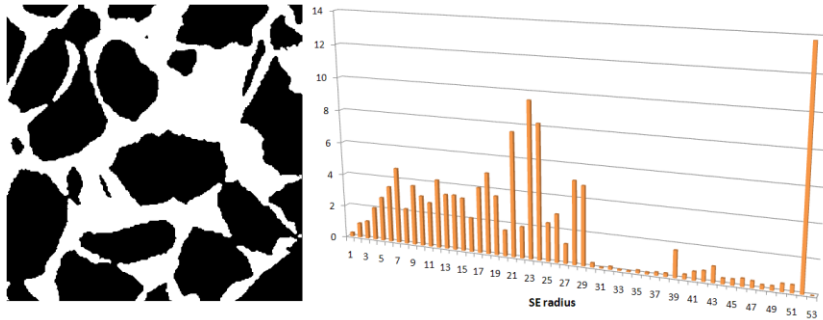


Figure 2.20: A binary image, on the left, and its dimensional curve, on the right.

In Figure 2.21 a dimensional curve is shown for only six macro-classes, in which all others are grouped. In particular, the red class groups objects intercepted by a spherical SE of radius $r \leq 3$ pixels, while the orange, yellow, green, and cyan correspond, respectively, to radius ranges [4-5], [6-15], [16-25], [26-35] and finally, the blue class groups objects intercepted by spherical SEs with radius $r > 35$ pixels.

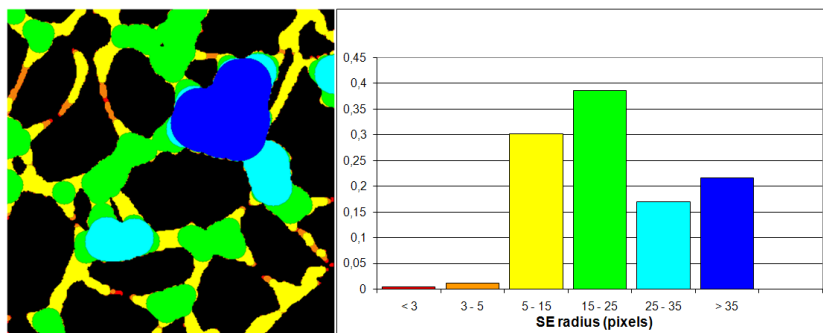


Figure 2.21: A 2D image and its dimensional curve for only six macro-classes.

In this way and thanks to “successive openings” algorithm (or its alternative version) we can identify all size

classes of the objects represented. In other words, we have partitioned the entire space according to the SE diameter.

2.3.2. Connectivity curve

Despite the rich information content, the size distribution does not take into account the manner in which objects are interconnected and the specification of “structure” requires also topological descriptors to characterize the connectivity, as well as the shape of the spatial configurations. The connectivity of a geometric body, with a net-like structure such as porous media, is characterized by its geometrical topology and requires necessary 3-dimensional analysis.

Given an images volume, we propose to measure objects connectivity by propagation methods [45] applied on foreground network after each step of *opening*, and with reference to couples of opposite edges of the VOI. In practice, the proposed connectivity algorithm includes three distinct phases:

- 1) identification of the connected components that link pairs of VOI opposite sides;
- 2) calculation of the residual volume;
- 3) application of *opening* to remove size classes less or equal to the spherical SE diameter.

These steps are repeated for each increasing value of the SE diameter, until all size classes are extinct.

Therefore, the evaluation of connectivity consists primarily in the individuation of any free paths that connect two opposite face of the cube that represents the volume of interest, see Figure 2.22.

The process of connected components identification is based on the labeling concept. It consists in assigning a label to each voxel in the image so that all voxels belonging to the same object are characterized by the same label.

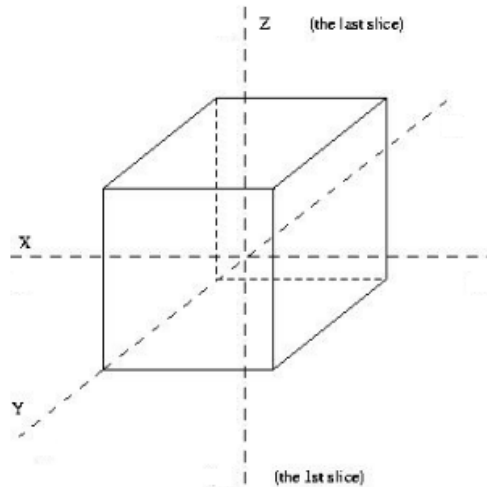


Figure 2.22: Representation of VOI in 3D.

It should be noted that the labeling result depends heavily on the discrete metric choice. In particular, in 3D case, for each point p , three different neighborhoods exist: $N_6(p)$, if one consider only voxels adjacent to the p six face, $N_{18}(p)$, if in addition to the six faces, the twelve edges are also considered, or $N_{26}(p)$, if one consider the six faces, the twelve edges and the eight corners. In practice each of these neighborhoods determines a different "proximity configuration", so if one choose $N_6(p)$ neighborhoods, then two voxels belong to the same object only if they have a face in common, but if one prefer $N_{26}(p)$ neighborhoods, they could share just a corner or an edge. In Figure 2.23 (a), (b) and (c) N_6 , N_{18} and N_{26} proximity configurations are represented respectively.

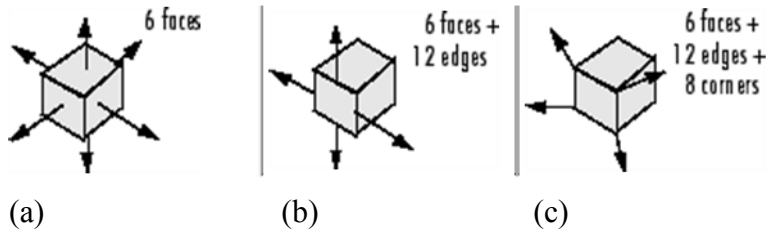


Figure 2.23: Proximity configuration: (a) N_6 , (b) N_{18} , (c) N_{26} .

Since porous media present very irregular structures we prefer the $N_{26}(p)$ neighbourhood by which it is possible to identify even very asymmetrical objects.

After labeling, only the connected components, along the propagation direction, are stored and this residual volume is computed. At this point, the first dimensional class is eliminated through the *opening* operator and the cycle restarts with the connected components analysis, that we call propagation. If any objects are still connected, this new volume fraction is computed and an *opening* of larger radius is implemented. The algorithm goes on until no connected components are identified or no size classes remain. In Figure 2.24 we illustrate the connectivity analysis algorithm flowchart.

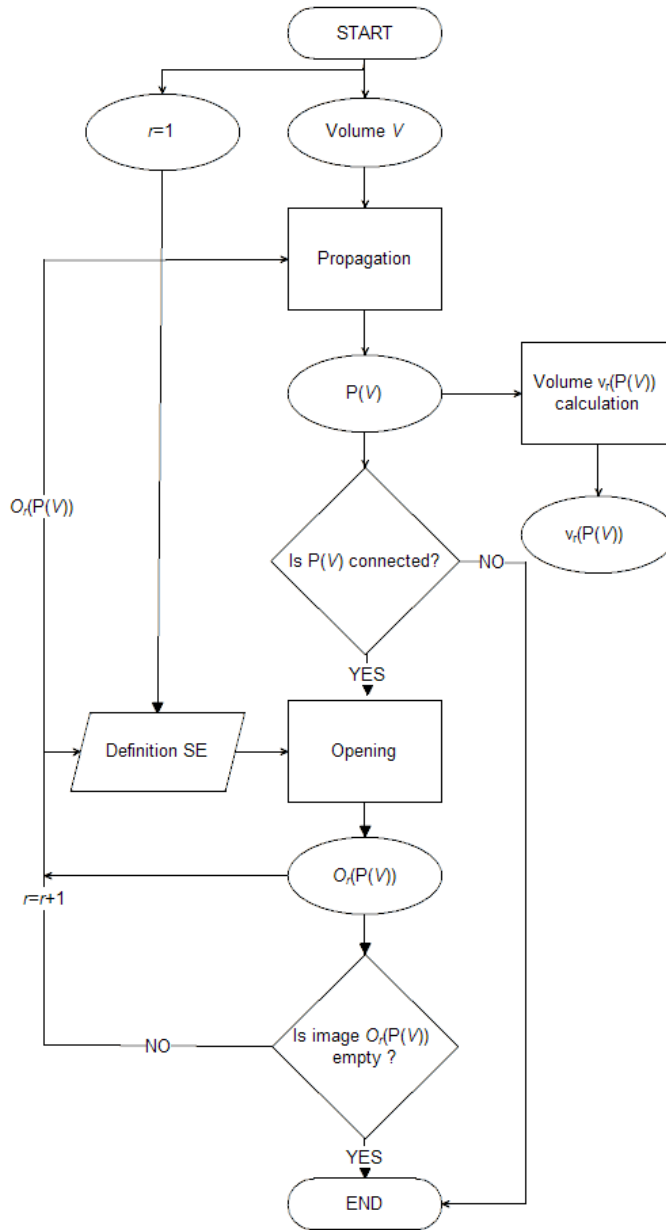


Figure 2.24: Connectivity algorithm flowchart.

These operations allow to draw one or more curves, one for each direction, called connectivity curves (or percolation curves), which indicate the percentage of the connected objects, at a given diameter, along two opposite sides of a VOI. For example, if we consider the two dimensional image shown in Figure 2.25 (a), it displays 4 objects that are partitioned, by “successive openings” algorithm, in 4 macro-size classes explicated in a color code. If we choose the vertical axis as connectivity direction, the propagation analysis confirms that only two object are connected from top to bottom, see Figure 2.25 (b). At this point, the connected objects area represents only the 27% of the total objects area, as reported on the curve shown in Figure 2.27.

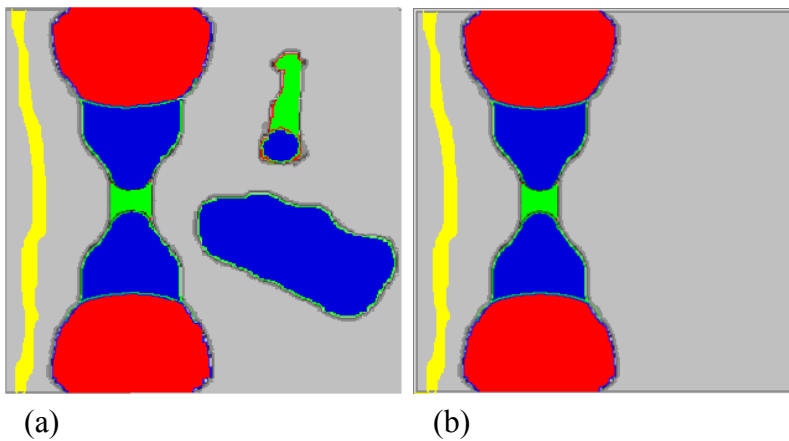


Figure 2.25: (a) Original image; (b) connected components from top to bottom

Suppose to filter the connected objects image, by *opening* operator with a spherical SE of radius $r=5$ pixels. The yellow size class is then intercepted and only one object is now connected from top to bottom, see Figure 2.26 (a).

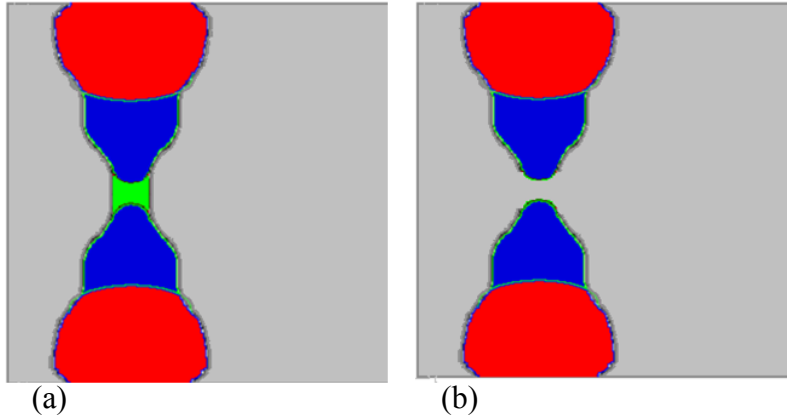


Figure 2.26: (a) Image of connected objects after *opening* with $r=5$; (b) image of connected objects after *opening* with $r=10$.

The area of this connected objects represents only the 22,5% with respect to the total objects area in the original image. If we choose a bigger SE, with a radius of $r=10$ pixels, the *opening* operator removes the green size class, breaking off definitively the connectivity, Figure 2.26 (b).

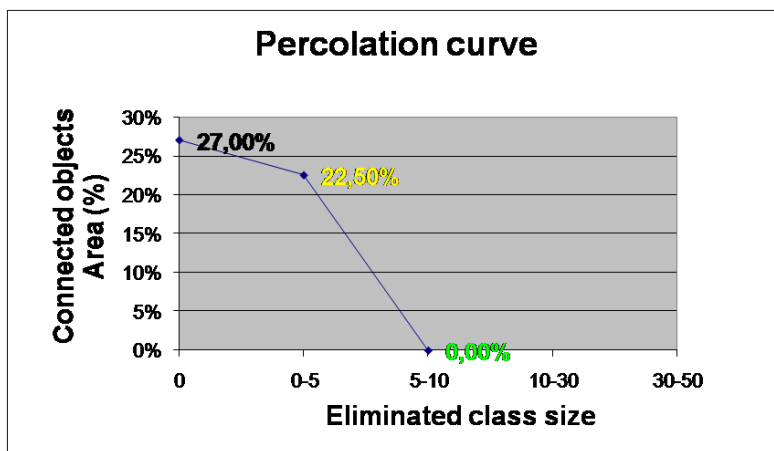


Figure 2.27: Percolation curve of a 2D example image.

As we have shown through a 2D example, once chosen a propagation direction, we have constructed the percolation curve by valuating the connected objects volume percentage with respect to SE diameter. We note that by connectivity analysis, the throat threshold values for the network is also identified. It is a critical diameter above which no connectivity and, then, no fluid passage is allowed anymore for the porous medium under analysis.

2.3.3. Effective porosity identification

The last operator explained, before going on to the experimental results, is the effective porosity, that is the porosity fraction really interested in passage of fluids. This problem is characteristic of some application areas particularly interested in the fluid dynamic phenomena that occur within the porous media.

In a porous system affected by passage of fluids, some preferential pathways are developed, based on the distribution of voids, i.e. the porosity. In practice, the fluids flow along certain directions rather than others, depending on the pores and throats size. In fact, only part of the pore phase in a porous medium participates in fluid dynamic processes. In particular, the closed pores located after a throat, even connected, do not participate actively in these processes and it is preferable to exclude them from the analysis. In this case, our goal is to develop an automatic procedure for identifying and removing this type of porosity, rather than manually locate these areas.

For this purpose, we use some morphological transform for binary images: “hit o miss transform” and “watershed transform”. In the following we briefly describe these morphological transforms in order to provide the basis to fully understand the proposed effective porosity identification technique.

2.3.3.1. Hit or miss transform

The “Hit or Miss” transform is used to identify specific patterns within an image and it is the basis of many other operators derivable from it. It is defined by:

$$A \circledast T = (A \ominus B_1) \cap (A^c \ominus B_2) \quad (22)$$

A point is in the hit-or-miss output if and only if B_1 translated to the point fits inside A and B_2 translated to the point fits outside A . It is assumed B_1 and B_2 are disjoint, for otherwise it would be impossible for both fits to occur simultaneously [46].

Rather than define two SEs, it is frequent practice to write a single template and to mark as foreground (0) pixels in the template used for the hit structuring element B_1 , mark with background (1) those used for the miss structuring element B_2 , and simply not mark those pixels used for neither. We call these “don't care” pixels (see Figure 2.28).

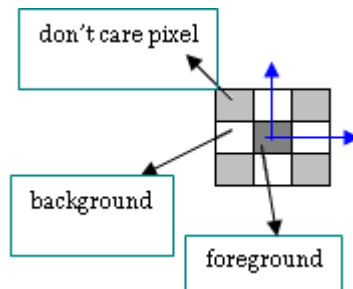


Figure 2.28: *Hit or Miss* template $B=(B_1, B_2)$.

Various morphological algorithms depend on the hit-or-miss transform, such as the thinning operator.

It is a morphological operation usually used to remove some foreground pixels from the binary image, or for reducing

the objects thickness. It is commonly used for the object skeleton extraction.

These procedures (skeletonization) can be further improved using a variant of thinning operator, called pruning. Algorithms based on thinning, in fact, may provide an inaccurate result, for example, in some cases (see Figure 2.29, on the left), the presence of small "fuzz", or "dead arm" is noted. The pruning algorithm is able to identify and then remove these "fuzz" (see Figure 2.29, on the right).

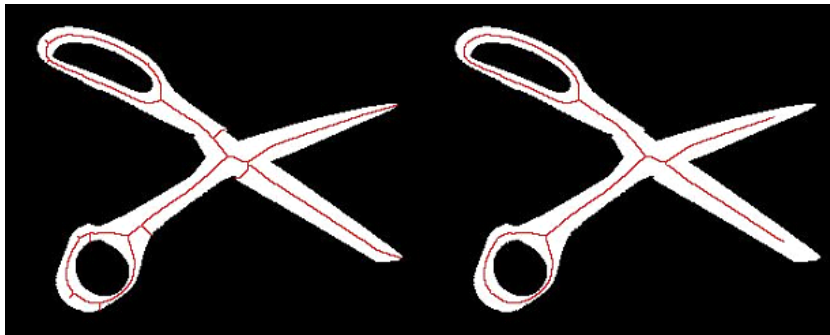


Figure 2.29: Thinning (left); pruning (right).

2.3.3.2. Watershed transform

The watershed transform is often used as key building block for morphological segmentation. In particular, a segmentation methodology for gray-scale images results from applying the watershed transform to the morphological gradient of an image. For this reason, watershed [47] [48] has become highly developed to deal with numerous real-world contingencies.

Perhaps the most intuitive formulation of the watershed transform is the one based on a flooding simulation. Consider the input gray-scale image as a topographic surface, Figure 2.30 (a). The problem is to produce the watershed lines on this surface. Suppose that every local minimum is perforated and the entire topography is filled from below, leaving the water go back through the holes uniformly, Figure 2.30 (b). When the

water risks to spill over from the different basins, a dam is built to prevent the merging, Figure 2.30 (c). Water can reach levels where only the tops of these dams are visible, Figure 2.30 (d). These dams correspond to the contours of the watershed lines.

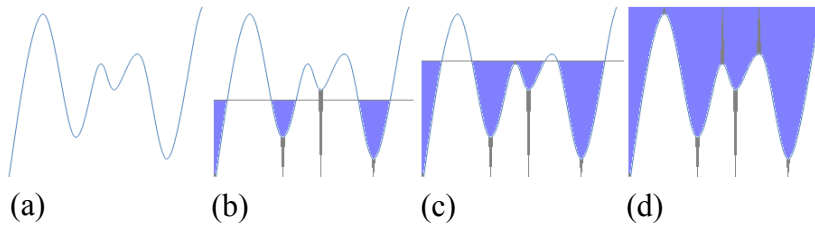


Figure 2.30: (a) Input signal, (b) initial flooding, (c) a dam is created when water from different minima is ready to merge, (d) final flooding.

2.3.3.3. The effective porosity identification algorithm

The proposed algorithm for the effective porosity identification is based on the operators just described, skeletonization and watershed.

Starting from the original volume, the z -connected volume is extracted, that is a volume with only the objects connected along z direction. In fact, for the effective porosity identification it is implicit to consider fluid passage, and only connected objects are interested from this process. The skeleton of the z -connected volume is then computed. It is an alternative representation of the interested volume, but more compact and easy to handle. Furthermore, if followed by pruning, the image skeleton is a very useful illustration of the original image. In Figure 2.31 as example, a z -connected volume and its corresponding pruned skeleton are shown.

We note that only the principal paths are represented, while the secondary paths are pruned. At this point, the problem is to reconstruct the effective porosity volume, because the skeletonization is not invertible.

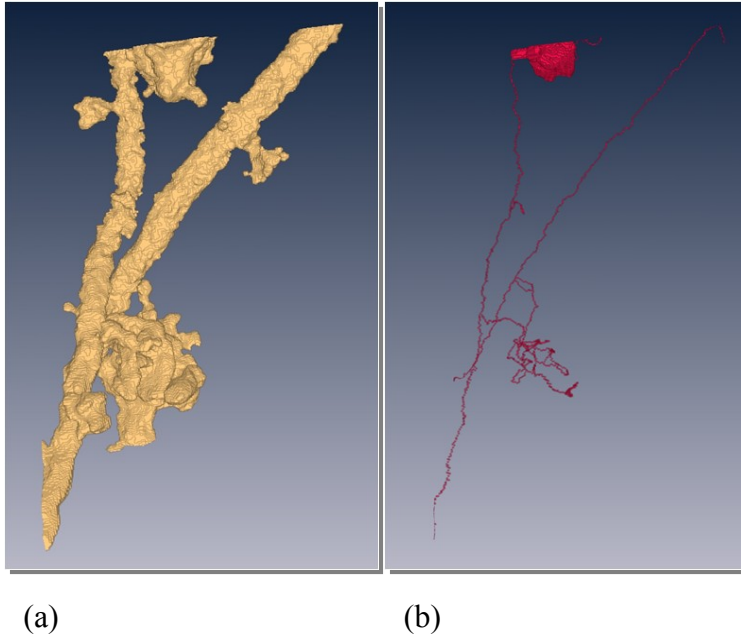


Figure 2.31: (a) Z-connected volume, (b) skeleton.

The ultimate goal of this procedure is to delete the porosity fraction that is not involved into flow dynamic processes, and, in particular, porosity which rises after throats. For this reason, we use the watershed algorithm to construct watershed lines. They pass through every throats present in the volume, included those we are interested in. Figure 2.32 (a), depicts the z -connected volume segmented by watershed lines. Now, intersecting these two types of information, the skeleton and the watershed lines, we are able to reconstruct the effective porosity volume, see Figure 2.32 (b). This dataset is very similar to the z -connected one, but we note that in this case, the porosity clusters after throats are effectively erased.

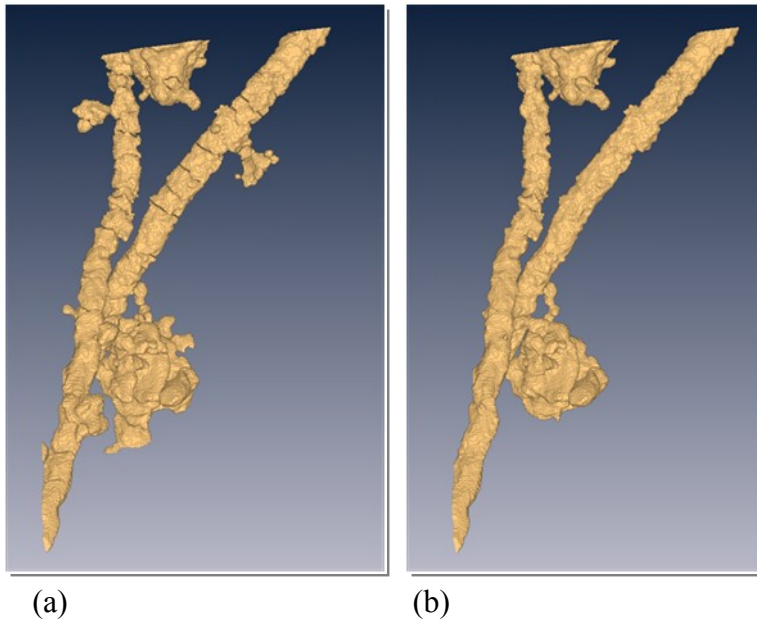


Figure 2.32: (a) Z-connected volume segmented by watershed lines, (b) effective porosity volume.

2.4. Advances in geo-sciences

Pore geometry imaging and its quantitative description is a key factor for applications to the study of physical, chemical and biological soil processes. For many years photos from flattened surfaces of undisturbed soil samples impregnated with fluorescent resin and from soil thin sections under microscope have been the only tools available for exploring pore architecture at different scales. Earlier 3D representations of the internal structure of the soil based on not destructive methods

have been obtained using medical tomographic systems (NMR and X-ray CT). However, images provided using such equipments show strong limitations in terms of spatial resolution. In the last decade very good results have then been obtained using imaging from very expensive systems based on synchrotron radiation. More recently, X-ray Micro-Tomography has resulted the most widely applied technique showing the best compromise between costs, resolution and size of the images [49]; and actually enhancing the potential to address soil processes related to real applicative problems. Thanks to a desktop X-ray micro-tomograph available at CNR ISAFOM in Ercolano (Italy), many soil samples have been scanned and analyzed for this thesis work. In the following, we report some experimental results obtained for such samples.

2.4.1. Experimental results

Established collaborations with other research centers have stimulated a diversified study of soil samples, looking each time at one of its multiple aspects. Below we describe only some of these.

2.4.1.1. In agricultural practices

One of the aims of many researchers is to investigate the link between soil pore geometry and agricultural practices. In this section we focus on the changes of soil surface structure due to three different irrigation practices under study in a vineyard area in the basin of the Mendoza river (Argentina).

Undisturbed soil samples were collected at the experimental farm of the Instituto Nacional de Tecnología Agropecuaria located in Chacras de Coria, department of Luján de Cuyo, Mendoza, Argentina (32° 59' S, 68° 52' W, 920.82m a.s.l.). It is an alluvial area in the basin of the Mendoza river where furrow irrigation is largely used in vineyards. Soil shows

a silty-loamy texture, a very low organic matter content and is rich in potassium and phosphorus [50]. In the experimental vineyard three irrigation practices were used: furrow irrigation (LT=labranza tradicional), drip irrigation with no tillage (LC=labranza cero) and irrigation by submersion with grass covered surface (CV=cobertura vegetal). In this study three subsurface sample volumes (about 30 cm³) are examined. Solid and pore phase of the three soil samples are shown in Figure 2.33.

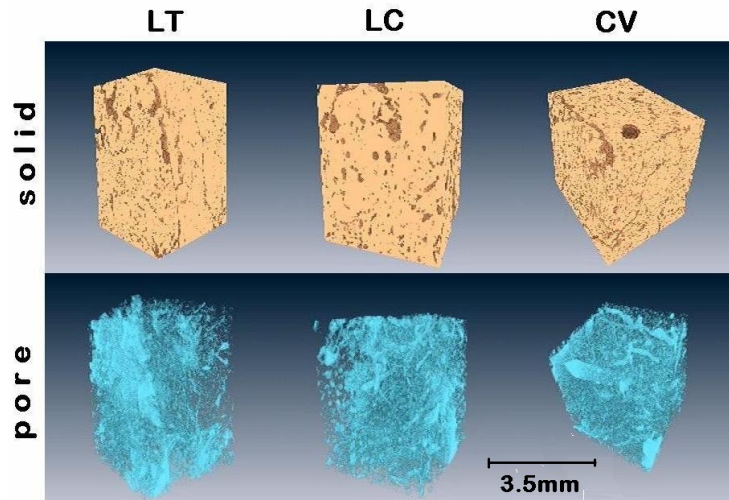


Figure 2.33: Visualisation of the solid and pore phase of the three samples at 10 micron image resolution. Volumes are cubes with side of 3.5mm.

Cubic regions of interests (ROIs) having side of 3.5 mm have been visualised and analysed. The results of the pore size distribution and connectivity are shown in Figure 2.34 and Figure 2.35, respectively.

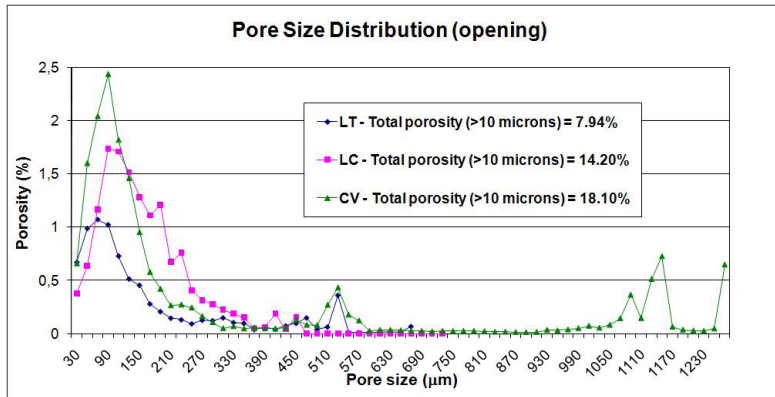


Figure 2.34: Pore size distribution of the three samples computed by “successive opening”. Porosity under one voxel has not been taken into account.

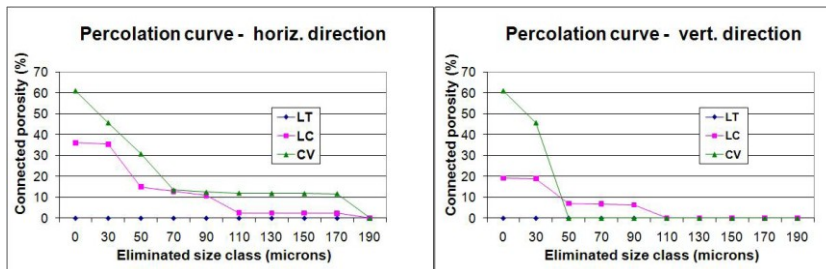


Figure 2.35: Horizontal and vertical pore connectivity (>10 microns) evaluated by the “percolation curve”.

Differences in porosity values (see the box in Figure 2.34) highlighted the compactness of the sample from the furrow irrigated plot (LT). This showed also a narrow pore size distribution around the modal value of 90 microns and a porosity peak around 550 microns due to presence of non-continuous cracks (see Figure 2.33); no continuous paths (larger than the voxel resolution) resulted in the pore network (see LT line in Figure 2.35). The CV sample (water submersion with grass covered surface) showed a higher and slightly wider pore size distribution around the modal value of 110 microns; porosity peaks around 550 microns and in the range between 1000 and 1300 micron are due to the presence of large tubular

pores left by the roots of the grass cover. In the LC case a multi-modal pore size distribution resulted in the range 0-500 microns, indicating the highest heterogeneity of pores in this size range. Complexity of the pore space organization can be generally considered as a good indicator of soil physical quality due to, for example, the plurality of habitats available for microbiological activity and the better effectiveness of water and air flow for the functioning of the roots.

Percolation curves (Figure 2.35) indicated that the pore network of both LC and CV samples were more connected in horizontal than vertical direction. In the LC case 35% and 20% of total porosity resulted to be connected in horizontal and vertical direction, respectively while percolation thresholds were of 190 and 110 microns, respectively. In the CV case 60% of porosity resulted to be connected in both vertical and horizontal direction, but the vertical percolation threshold showed a lower value of 50 microns. Therefore the CV sample, notwithstanding its highest porosity, exhibited narrower necks in vertical direction than in the case of the LC sample, allowing to presume a worse fluid flow in the pore network.

Results shown in this study are part of a multi-approach more general investigation to evaluate convenience in changing the traditional irrigation practice in the area of the Mendoza river (Argentina), in order to enhance water use efficiency and crop quality. They overall demonstrate the useful contribution of the 3D pore image analysis in understanding the consequences of the three alternative practices under study on the subsurface soil pore architecture.

PROCESSING TIME

Before moving to the next experiment, we dedicate a few words to the processing time. In Figure 2.36, we report a curve related to *opening* time execution for the LC sample mentioned above. In gray we report the trend line, which shows that the execution time grows in a more than quadratic way.

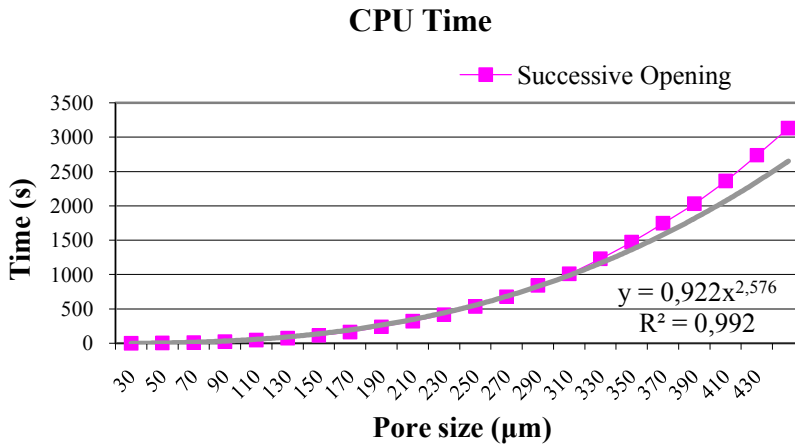


Figure 2.36: Experimental (pink) and trend (gray) execution time for LC sample.

Using simplified procedures explained in §§2.2.3.1, 2.2.3.2, one could obtain the PoSD curves in reduced time. In Figure 2.37, processing time in log-axis is plotted for the three versions of “successive openings” algorithm implemented. It is clear that the *opening* simplified version, with an octagonal SE, is faster than the traditional version. By looking at the analysis results, however, one can appreciate that the alternative version, using distance transform and *dilation* operator, is not only the fastest, but also more accurate than the simplified one.

As mentioned before, the simplified version of “successive openings” uses a non-isotropic SE, therefore the analysis, such as PoSD, leads to approximate results. In Figure 2.38, in particular, we note that the simplified version overestimates the small pores, while larger ones are underestimated. The curve of the simplified version, in fact, initially climbs over the others, but as the number of cycles increases, is almost always below the other ones.

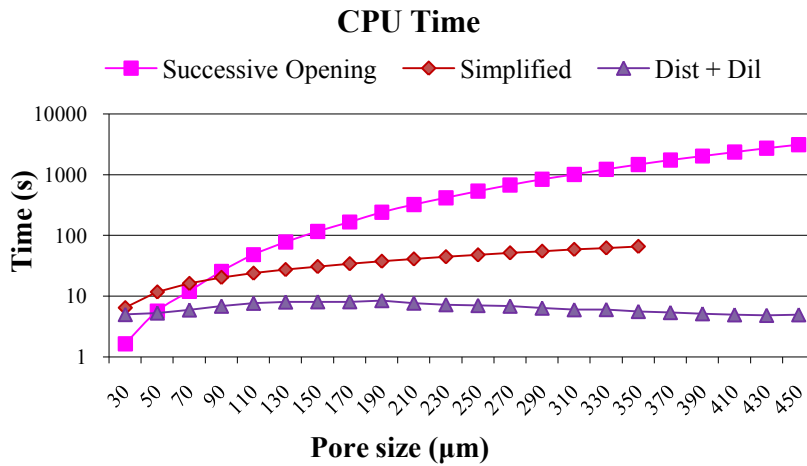


Figure 2.37: CPU time for the three versions of “successive openings”.

Instead our fast version of "successive openings", gives very accurate results. Only during the first *opening* steps, the two curves differ slightly. Probably, because initially the object contours are still very jagged, and the differences in behavior between *opening* and *dilation* are more obvious.

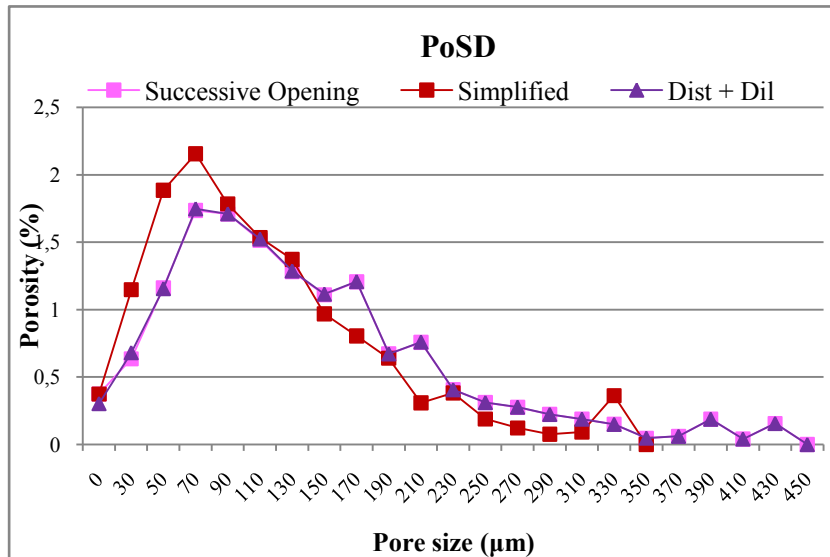


Figure 2.38: PoSD curve of an LC sample obtained by three different algorithms.

2.4.1.2. Soil physical processes

Highly eroded environments can be stabilised using plant structures which often produce crusted soil layers. In the steppified desert region of Shapotou (China) a vegetated protection system was progressively established since the 1950s up to 2004 [51]. Initially, a sand barrier was built with woven willow branches or bamboos to reduce wind *erosion*. Behind the sand barrier, straw chequerboards (wheat or rice straw) were installed, usually with sections of 1 m² area. The fixed sand surface led to the formation of very different microbial soil crusts although applied on the same soil according to the age of the straw structures.

Soil crust samples, named T_2004, T_1989, T_1964, have been collected from three sites in which the protection system from *erosion* date back to 2004, 1986 and 1958 respectively. Portions of about 1,5 cm in diameter have been scanned with the Skyscan 1172 x-ray micro-tomograph. A smaller portion of not stabilized natural sand material has also

been reconstructed at a resolution of $3,5 \mu\text{m}$ in order to have a reference result (T_ref) on the initial conditions of the soil crust formation process.



Figure 2.39: Soil crust samples, T1, T2 and T3.

In Figure 2.39 are pictures of the soil aggregates scanned at the three stages of surface microbial crust colonization. T_2004 shows many surface inflorescences with very thin roots, which disappear in T_1989 and T_1964 samples. These latter are more compact than T_2004. T_1989 is the thinnest and shows a “wave” shaped surface while T_1964 looks significantly thicker than the others. In Figure 2.40 the 3D reconstructions are also visualized. T_ref is clearly a loose homogeneous sand not showing any aggregate structure.

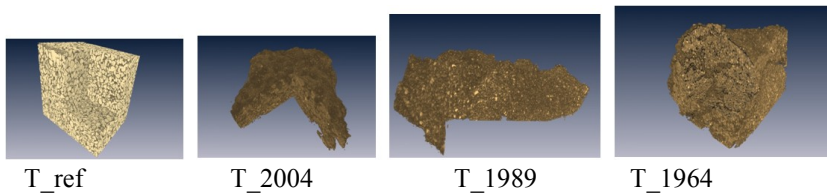


Figure 2.40: Soils reconstructions.

Pore Size Distribution, Figure 2.41, confirms what is observed above about compactness thickness and shape of soil crust. T_ref dimensional curve is strongly unimodal with a very short range of pore sizes. Comparison shows that a progressive decrease of smaller pores has resulted at increasing age of the

soil crusts. Presence of larger pores is also evident in crusted samples.

3D PoSDs are also represented in Figure 2.42

Differences in total porosity are only partially due to different resolution between the 3D images of the samples.

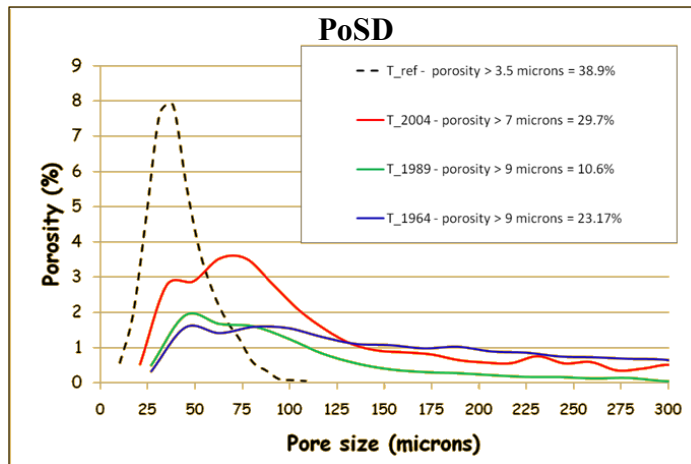


Figure 2.41: PoSD comparison.

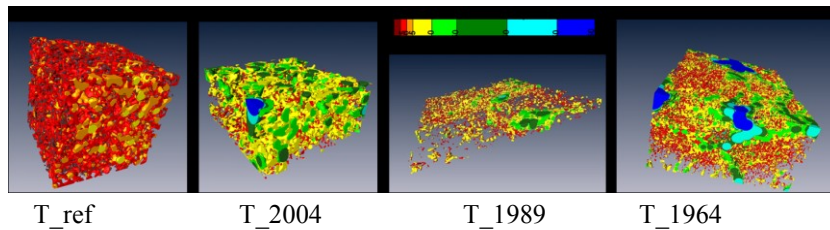
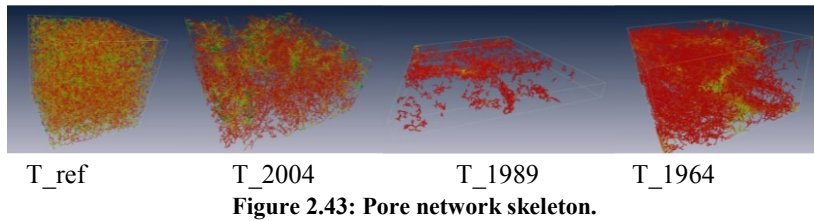
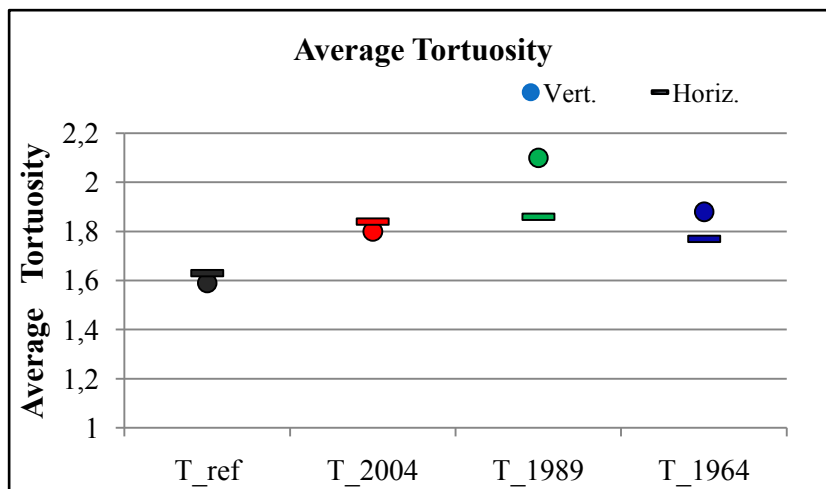


Figure 2.42: 3D PoSD comparison.

The skeleton of the pore network (Figure 2.43) has also been obtained according to procedure of the Pore-throat Analysis proposed by [28]. All paths of the medial axis connecting opposite faces of the four volumes have been identified.



For each path the tortuosity value is calculated according to the definition (see note 3).



Crust aggregates show a general increase of average pore network tortuosity, see Figure 2.44, reaching the maximum value in the T_1989 case. T_1989 and T_1964 exhibit also a significant anisotropy of the tortuosity. In such cases the pore network has resulted more tortuous in vertical direction.

In conclusion we can say that X-ray micro-CT imaging coupled with 3D image analysis based on specific procedures for porous media have provided a very accurate quantification of

the internal structure of microbial soil crusts due to stabilized sand dune of different age.

2.5. Advances in biology

Osteoporosis is the most common metabolic bone disease worldwide. It is mainly a result of decreased estrogen levels, and the disease is associated with a markedly increased risk of skeletal fractures. Current diagnostics of osteoporosis are largely based on the measurements of areal bone mineral density (BMD [g/cm²]), using dual energy X-ray absorptiometry (DXA) of the proximal femur or the lumbar spine. However, BMD is only a moderate predictor of fracture risk. In general, a fracture occurs when the strength of the bone is exceeded. A variety of factors determine the strength of bone, including BMD and the microstructure of the trabecular bone. Quantification of these features using high-resolution micro-CT imaging has become an important research topic.

Osteoporotic bone is typically characterized by a lower bone volume fraction and trabecular number, as well as higher trabecular separation compared to the healthy bone.

In order to verify the sensitivity of the proposed indicators to the pathological states of bone, in the following we present a morphometric study on two bones samples.

2.5.1. Experimental results

Two bone samples, one taken from a healthy donor, hereinafter called 'sample A' and the other, 'sample B', from a donor suffering from a metabolic bone disease, are analyzed.

At a preliminary visual inspection, the two samples have different characteristics: the structure of the first sample, 'sample A', appears homogeneous and compact, with similar trabeculae

in size, they vary only slightly along different spatial directions. The 'sample B' seems rather heterogeneous, with trabeculae very thin or on the contrary quite thick. Furthermore, the elements arrangement is messy and does not show any spatial isotropy property.

Beyond physical condition of the donor, the reason for this structural difference may well depend even on the original site from they are levied, but at the analysis time this information is not known. For this reason the results are discussed assuming that the samples are taken from comparable sites, if not the conclusions should be revised, adding the missing information.

2.5.1.1. Trabecular Size Distribution (TrSD)

In Figure 2.45, the two dimensional curves of samples are plotted.

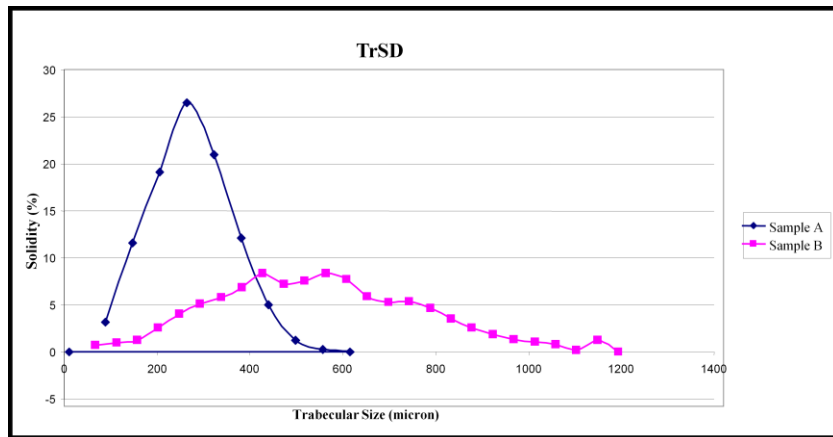


Figure 2.45: TrSD comparison.

The first sample TrSD is completely consistent with the comments made after simple visual inspection. The trabeculae diameter variability is rather limited: the distance between solid

walls, in fact, varies only between 88 μm and 616 μm . This is consistent with the sample homogeneity. Furthermore, most of the trabeculae, almost 27%, is characterized by a diameter of about 264 μm , which can be considered a characteristic value of the sample analyzed. In other words, the sample mechanical and resistance properties are then assigned to this size class.

Instead, 'sample B' TrSD looks very different from the first one. It is easy to note that trabeculae are characterized by very different diameter values. In fact, the variability ranges from just 78 μm to about 1150 μm . Moreover, no one value is characteristic, because the curve is not strictly unimodal, and just over 8% of the total solid volume reaches its maximum.

In 'Sample B', trabeculae have diameters also quite high, that are not present in the 'Sample A' (healthy donor). They are generally more robust in the second sample, but there are only few specimens for each size class. In this way the mechanical and resistance properties are concentrated in a few points and not uniformly distributed within the bone volume.

2.5.1.2. Connectivity analysis

The connectivity curve is calculated to evaluate the presence and the characteristics of potential paths between two VOI sides. It is better to clarify that at the analysis time, however, the original samples orientation directions and angles were not known, for this reason the names assigned to directions are only indicative. Probably more precise indications about the samples structural properties could be assess from the knowledge of this information.

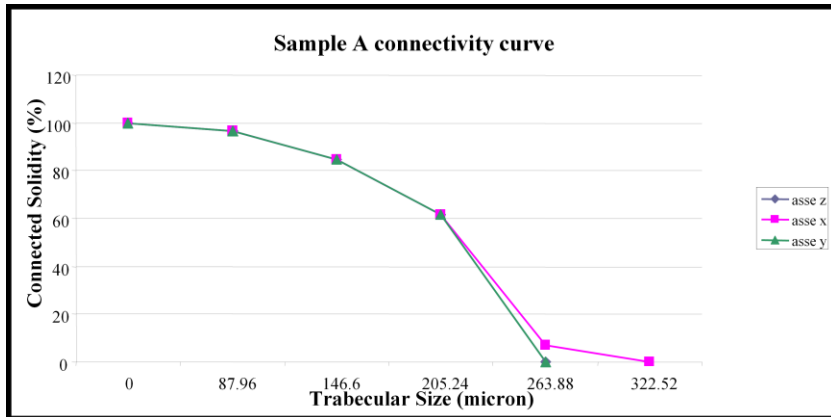


Figure 2.46: 'Sample A' connectivity curve.

The first sample connectivity curves show that the trabeculae are strongly connected in all three directions considered (Figure 2.46). This implies that, if a disease eliminate trabeculae with a small diameter, for each orientation, links between the opposite faces of VOI are still present. By increasing the removed diameter, however, the connectivity decreases more and more. In particular, the diameter of about 205 μm , it can be considered a measure limit, in fact, taken this class size, there is a lowering of about 60% for the connectivity. Therefore, the critical diameter is equal to 264 μm so, delete this class, in VOI is not present any form of connectivity. This result is fully consistent with the comments on TrSD: trabeculae characterized by a diameter of 264 μm are more than 25% respect to the total solidity, and they are also responsible for the sample connectivity properties. Trabeculae with a diameter greater than this, do not actively participate in load resistance processes.

By examining the second sample connectivity curves (Figure 2.47), we can express some interesting considerations.

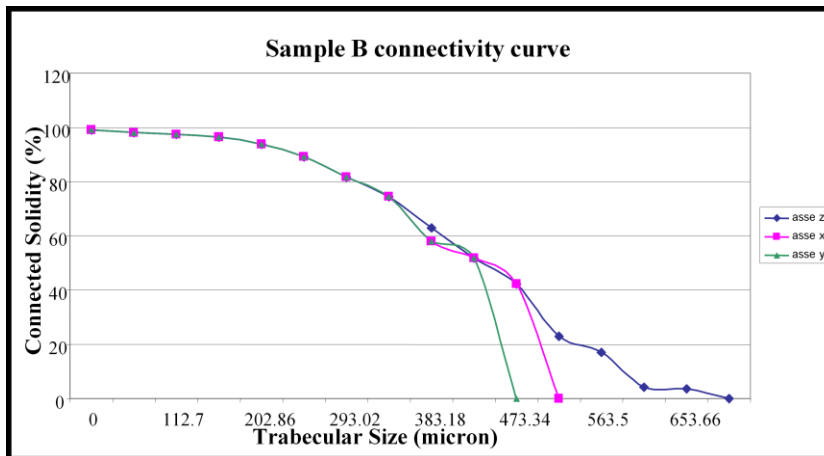


Figure 2.47: 'Sample B' connectivity curve.

First, the structural behavior is slightly anisotropic, just as in fact pointed out earlier. In particular, along direction called z axis, connectivity depends from large trabeculae diameter values. Although the volume seems very connected, in this case, its connectivity rapidly decreases. Given the wide size classes variety, with the trabeculae diameters of $1150\ \mu\text{m}$, surprisingly in directions named y and x , connectivity vanishes already for a diameter of approximately 473 and $518\ \mu\text{m}$, respectively. So although there are fairly robust structure, connectivity analysis shows that, in practice, the carriers trabeculae diameter is considerably lower.

2.5.1.3. Conclusion

Although suffering from the useful information lack, the presented analysis proves that the proposed indicators reflect the physiological or pathological nature of bone tissue samples.

In particular, the dimensional curves return the trabecular size classes composition. A unimodal pattern is associated with a homogeneous structure ('Sample A'), while the presence of a large number of size classes is consistent with the bone sample affected by osteoporosis ('Sample B').

The connectivity curves show also that, in the healthy sample, the critical diameter above which there is not connectivity is also a characteristic VOI parameter. On the contrary, for the sample with osteoporosis, the connectivity is assigned to size classes smaller and less frequent than the varieties present in the volume.

Chapter 3

Image denoising

The noise is an unpredictable perturbation which disturbs a signal causing random fluctuations of the observed variables. Generally speaking, it is an issue of considerable importance in any acquiring and processing data system, especially imaging techniques. The scientific literature offers a plethora of denoising functions often included in commercial software as tools to support and simplify the extraction of significant information from noisy images.

In fact, image denoising has been the object of intense research from the very beginning of the digital era and an enormous variety of procedures for image denoising have been offered, most of which have been or can be adapted to deal with CT and microCT images. For the correct application of the any denoising filter method, however, the knowledge of noise characteristics is an essential precondition.

In this chapter we will initially focus on CT⁹ noise, because it poses a difficult problem to the traditional image denoising techniques. Then a denoising method for colored noise is proposed.

⁹ The literature concerning micro-CT images is not very large given its recent introduction, so below, with some exceptions, we will refer to CT imaging system, which have been the object of more extensive studies.

3.1. CT noise

A CT or micro-CT image is the ultimate result of a complex measuring chain in which each step is also a noise source. Thus, in a generic CT image it is possible to consider the noise as the sum of different contributions, one for each different stages of image generation process. Indeed, the following main noise components are identified in tomographic images: quantum noise due to the fluctuation in x-ray detection; electronic noise caused by electronic devices (even if that can be considered negligible with respect to quantum noise), and structured noise arising from the reconstruction process.

The quantum noise is considered the major component of tomographic noise and it is caused by X-ray energy transmission in discrete units, the photons. Indeed, the X-ray sensor response is actually the result of the detection of a finite number of photons that can change from one measurement to another, not because of device inadequacy, but for the statistical fluctuations arising from the counting process. The main cause of the quantum noise is thus identified in the discrete nature of X radiation. This clearly represents a fundamental limitation of the X-ray based imaging technologies, because it is necessary to increase the number of quantum detected, i.e. the radiation energy (the dose), to obtain a noise reduction.

In fact, we recall that the probability for a photon to be deviated from the original beam, by absorption or scatter (due to Compton effect) is a function of the photon energy and actually, the x-ray tube used in micro-tomography generates quanta having a spectrum of continuously variable energies. Unless one makes some simplifying assumptions, the problem of modeling the noise in projections is not trivial, since many aspects must be taken into account such as the energy-integrating detection processes, the non-uniform flux profiles and the data-conditioning processes. Despite various efforts [52] [53] [54], no model has been developed for the probability density functions (pdf's) of polyenergetic measurements and, usually, a

Gaussian distribution is assumed [55], based only on the central limit theorem for high-flux levels.

If for projections the noise models are really poor, for reconstructed images the situation is even less clear. In fact, due to reconstruction process, typically filtered backprojection method (see §1.1.2.2), and to other operations used to obtain the final image, the noise distribution is further modified. In particular, although noise at the detector can be assumed to be white, the reconstruction algorithm introduces some correlation. Additionally, noise in the CT image depends on the (unknown) signal to be reconstructed, which makes the analysis even more difficult.

Nonetheless, given the practical significance of this problem, many studies have been proposed in the literature under certain simplifying assumptions. In particular, the tomographic system noise characteristics have principally been considered for two aspects: the statistical uncertainty per pixel ([56], [57], [58], [59]), that assesses only the magnitude of local statistical fluctuations; and the noise power spectrum ([60], [61], [62], [63], [64], [65]) which describes the variance distribution as a function of spatial frequency.

From our point of view, we are interested to implement a technique for micro-CT image denoising, and for this reason we have experimentally analyzed the noise property of micro-CT data. In next sections, we discuss methodologies and obtained results.

3.1.1. Noise experimental characterization

With the collaboration of the CNR “ISAFOM” centre of Ercolano (Naples, Italy), an experimental protocol has been outlined for the micro-CT noise characterization.

First of all, to provide images containing the noise to be analyzed, we have produced and scanned a test object. In a cylindrical container of polypropylene (PP, with low absorption

coefficient) we have placed a homogeneous material of epoxy resin, typically used in thin section impregnation. Before scanning the sample, alignment procedures between object stage and source or detectors, are necessarily performed, to minimize the presence of artifacts. Moreover, to reduce other noise contributions, a prior acquisition of the background is completed, and later subtracted from the image obtained when the sample is placed. This acquisition is made with the same parameter settings used during sample acquisition.

In this study, we have chosen to work with a resolution of about 34,5 μm , that is relatively low for the system under investigation. Moreover, to reduce the beam hardening (§1.2.2) effect, we have used a aluminum filter of about 0.5 mm to block the soft component radiation, thereby only the hard one can pass. Finally, we have mediated the projections used in the reconstruction process on 12 realizations.

We have repeatedly acquired projection measurements of this test object, from an unchanged angle, for 16 times by a Skyscan 1172 desktop micro-CT scanner. For each acquisition, 50 images are reconstructed, of 1000x1000 pixels; they are represented on 8 bits, i.e. 256 gray levels, with no post-filtering, but for ring artifact correction. One of these images is displayed in Figure 3.1.

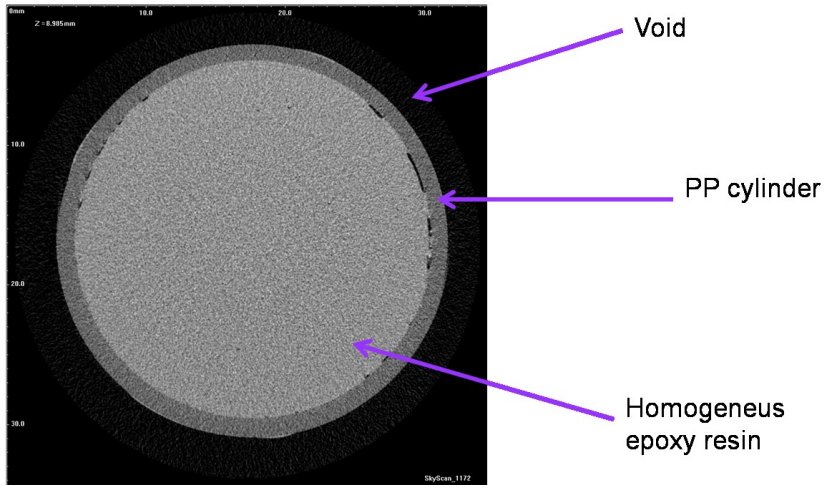


Figure 3.1: Test object reconstructed image.

To measure image noise, we have selected a square ROI of 512x512 pixels, entirely included in the homogeneous area, see Figure 3.2.

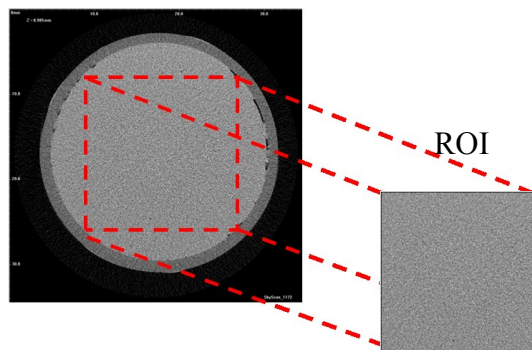


Figure 3.2: Selected square ROI.

Every image obtained in this way, is a noisy image, in other words, both signal and noise are contained, but we are interested only on noise. Considering that the homogeneous material is characterized by a single attenuation coefficient and

then by a single gray level value, the noise is obtained by subtracting the signal level from the noisy image.

To estimate the signal, we have averaged the central sections¹⁰ of all acquisitions, and we have estimated. In Figure 3.3, we report the gray level distribution of the mean image.

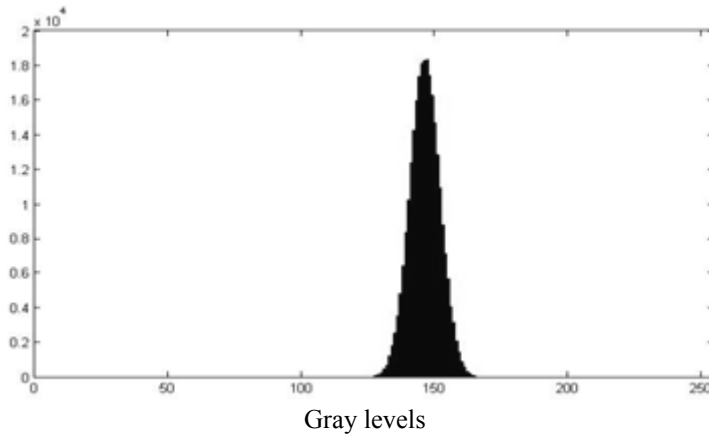


Figure 3.3: The gray level distribution of the mean image.

With reference to the experimental parameters chosen, the noise has an appearance like that shown in Figure 3.4 (a). The relative frequencies distribution of the pixels gray levels is shown in Figure 3.4 (b) (in blue) with comparison to corresponding Gaussian pmf (in red) generated from the same mean and standard deviation. The Kolmogorov-Smirnov test [66] confirms that the noise distribution of the reconstructed image has is approximately Gaussian, as some authors [67] [68] have already proposed for pixel image generated by CT scanners.

¹⁰ Because no thickness information has to be used to reconstruct the central section, in this case, possible geometrical distortion are avoided.

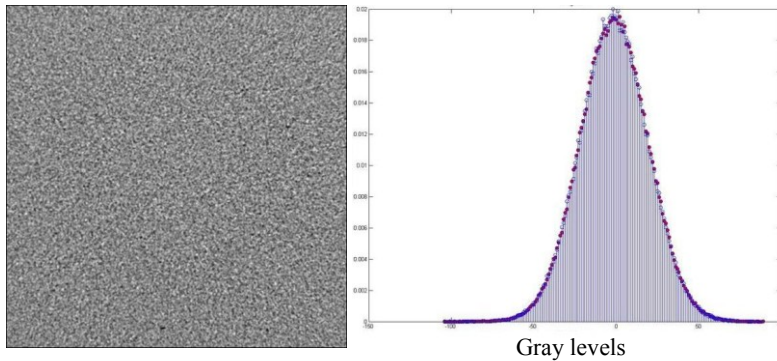


Figure 3.4: (a) Image of noise, (b) relative frequencies distribution of the pixels gray levels, in blue, and normal pmf, in red.

Finally, we assess the effects of correlation, induced by the reconstruction process, estimating the correlation coefficient variation along the rows and along the columns, see Figure 3.5.

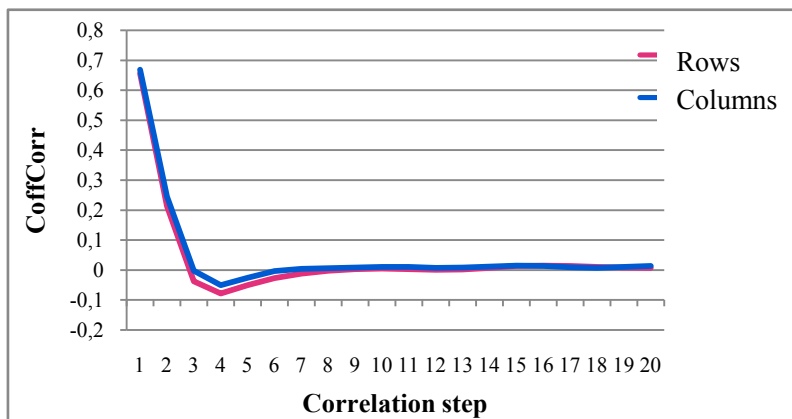


Figure 3.5: Correlation coefficient variation along the rows and columns.

The experiments show clearly that micro-CT noise is colored, as expected, and provide the correlation form. A denoising technique for correlated noise is then required.

3.1.2. CT image denoising: state of art

Given the issue relevance, especially for medical application, for years many denoising techniques have been proposed or adapted for CT noise suppressing. We will start with a short overview.

A first approach is to work on sinograms, before the image is reconstructed. By working in this domain, one can take advantage of the existing statistical models of the noise, deriving from the deep understanding of its physical origin and supported by statistical studies [69]. On the other hand, any action taken on the sinogram has consequences on the reconstructed image that cannot be easily predicted, such as the suppression of diagnostically relevant features. In most of the sinogram based methods, filters are adapted spatially in order to reduce the noise in regions of highest attenuation. Thus, the main achievement of these methods is the reduction of directed noise and streak artifacts. However, when the noise variance is nearly constant over all of the projections, these filters either do not remove any noise, or cause a noticeable loss of image resolution. In general, a moderate denoising of the sinogram can be useful, but a stronger action is not advisable, especially for low signal-to-noise ratios, in order not to put at risk important structures in the reconstructed image.

After CT-reconstruction, the situation is reversed: image structures are now visible, and their regularity can be exploited to guide the denoising process. On the other hand, the experimental studies show that the noise is object-dependent and non-white; with these premises, it is clear that denoising techniques developed under classical AWGN (additive white Gaussian noise) hypotheses should be considered with great care and that can easily fail or provide unconvincing results on CT data [70].

Most of the conventional denoising algorithms are based on linear smoothing filters, that is, low-pass filtering in the Fourier domain, but they not work very well with cone beam CT imaging. They may reduce significantly the power of noise, but

this is obtained by suppressing both high and medium frequencies (where most of the noise power is concentrated [71]) thereby affecting the sharpness of edges, rich in high frequency content, and possibly erasing altogether some thin structures. Some improvements may be obtained by resorting to adaptive filters, which try to locate and preserve edges, but these are quite complex and only partially effective; or to non-linear filters, like the median, which does a better job near the edges but works well only for impulsive noise, not the case of microCT images.

Significant improvements have been obtained in recent years by resorting to wavelet transforms, thanks to their many desirable properties, such as locality, sparsity and multiresolution. In 1994, Donoho and Johnstone [72] opened the way to wavelet shrinkage techniques. The main idea is to exploit the excellent energy-concentration property of wavelet transforms. Indeed, with typical images, generally smooth but for some localized edges, the transform concentrates most of the energy in a small number of large coefficients, while all other coefficients are almost negligible (that is the transform is sparse). White noise, instead, is evenly distributed by the transform on all coefficients, which remain all relatively small. A noisy image, therefore, presents in the wavelet domain a small number of large (signal dominated) coefficients, while all the rest (noise dominated) are quite small. By zeroing-out these latter coefficients, through a suitable thresholding, one removes most of the noise and can recover a remarkably clean image through the inverse transform.

Starting from this basic technique, referred to as hard thresholding, a number of improvements have been proposed, including soft thresholding [73] and more elaborate shrinkage schemes, the use of subband adaptive thresholds, and context-based techniques where dependencies between in-band and across-band coefficients are also taken into account [74].

In the last few years, a new approach has been gaining ground in image denoising field, known as nonlocal filtering, first formalized in the non-local means (NLM) algorithm

proposed by Buades, Coll and Morel [75]. The major breakthrough of NLM consists in selecting in a very sensible way the set of pixels used to estimate the true value of a target pixel, that is, not the pixels closest to the target, but those deemed to be the most similar to it. In practice, for each target pixel z^T of the noisy image $z(n)$, the surrounding patch P^T is extracted and compared with all patches P_i in a given neighborhood of the target. The patches that are more similar to the target patch, according to a suitable “distance” measure, are associated with the most relevant predictor pixels, that is:

$$z^T = \sum w_i z_i \quad (23)$$

where the weight w_i is a decreasing function of the distance $d_i=d(P^T, P_i)$.

The nonlocal approach turns out to be especially effective in the presence of edges and textures, when patches are well characterized and bring valuable information on the pixel context, providing a significant performance improvement w.r.t. conventional techniques both in the spatial and transform domain.

Following the success of NLM many variations have been proposed, among which the block-matching 3D (BM3D) algorithm [76], which appears to be the current state of the art in image denoising and restoration in general.

Although a thorough description of BM3D is out of our scope, we need to recall here its basic steps. The first action taken by BM3D, just like in NLM, is to locate similar patches by means of block-matching. Unlike in NLM, however, all such patches are then collected in a 3D structure which undergoes a decorrelating transform (typically wavelet) so as to exploit both spatial and contextual dependencies. Once a sparse representation is obtained, some form of shrinkage is used to remove noise components, before going back in the image domain. Since filtered patches can overlap, several estimates of

the same pixel are typically obtained, which are weighted to compute a “basic estimate” \hat{y}_{basic} of the denoised image.

At this point, the noisy image $z(n)$ undergoes the denoising process anew, with the difference that block-matching takes place on the basic estimate \hat{y}_{basic} of the clean image so as to obtain more reliable matches, and wavelet shrinkage is replaced by empirical Wiener filtering, with statistics computed again on \hat{y}_{basic} .

Both NLM and BM3D have been proposed in the context of AWGN image denoising and, therefore, work poorly in all situations where the noise cannot be considered Gaussian nor white. Nonetheless, the nonlocal approach keeps making full sense, and hence there is much interest in adapting the basic algorithms to such new conditions (see also [77] [78] [79]).

3.2. State of the art of non-AWGN denoising techniques

The problem of nonlocal image denoising in the presence of colored noise has been already addressed as well.

A version of NLM for colored noise (NLM-C) is proposed by Goossens et al. [80] where the noise is assumed to come from the linear filtering of white Gaussian noise. Given the impulse-response of the filter, and hence all noise statistics, the Authors replace the Euclidean distance, used originally to compute the similarity among patches, with the Mahalanobis distance which takes the noise covariance matrix into account. Alternatively, to reduce the computational load, they apply a prewhitening linear filter to the noisy image and use the resulting image to compute the weights by the Euclidean distance. Next, this prewhitened image is only used to compute the weights based on the Euclidean distance. Numerical experiments show NLM-C to provide significant improvements, both visually and in terms of PSNR, not only over basic NLM

(called NLM-W in this context) but also *w.r.t.* to some recent wavelet-based denoising techniques for colored: BLS-GSM [81] and MP-GSM [82].

Also BM3D has been already adapted [83], to the case of correlated noise. The Authors observe that when using the 2D and 1D transforms (T_{2D} and T_{1D}) to cross into a transformed domain, if they are orthonormal and the noise in the input image is i.i.d. Gaussian, then the noise in the T_{3D} -transform domain is also i.i.d. Gaussian with the same constant variance; but, if the noise is colored, then the variances of T_{2D} -transform coefficients are in general non constant. For this reason they computed the coefficients variances of a T_{2D} -transform (applied to an arbitrary image block) $\sigma_{2D}^2(i)$, $i=1, \dots, N_I^2$ where N_I is the block dimension. This fact is taken into account in various phases of the algorithm: by using a weighted block distance computed in the transform domain; by using a different shrinkage threshold for each coefficient; and by aggregating filtered blocks based on their expected noise level.

When determining the block-distance, to reduce the influence of noisier transform coefficients, the block-distance is computed as the l^2 -norm of the difference between the two T_{2D} -transformed blocks scaled by the corresponding standard deviations of the T_{2D} -transform coefficients.

After the best-matching, blocks are found and grouped together in a 3D array and collaborative hard-thresholding is applied. It consists of applying the 3D transform T_{3D} on the 3D group, hard-thresholding its spectrum, and then inverting the T_{3D} . To attenuate the colored noise, the hard-threshold is made dependent on the variance of each T_{3D} -transform coefficient as computed before (actually along the third dimension of a group the variance is the same).

After all reference blocks are processed, the filtered blocks are aggregated by a weighted averaging. The weight for all filtered blocks in an arbitrary 3D group is the inverse of the sum of the variances of the non-zero transform coefficients after hard-thresholding.

During the second step, the only modifications from the original BM3D filter concerns the use of T_{3D} -transform coefficients variances in the empirical Wiener filtering, and for the aggregation weight. Since the grouping by block-matching is performed on the estimate and not on the noisy image, there is no need to modify the distance calculation.

Based on the above ideas, we propose a new version of BM3D for correlated noise. We use the basic strategy of the original BM3D algorithm because of its strong rationale, but modify it in several steps to keep into account the actual noise statistics. In particular, we improve the block matching by resorting to image prewhitening, and the shrinkage (hard thresholding in the first step, and Wiener filtering in the second step) by taking into account the different noise variances of coefficients and improving their estimate.

3.3. The modified BM3D algorithm

Since the proposed algorithm is a modification of BM3D, we describe and discuss here only the differences *w.r.t.* the original algorithm [76].

The first and probably most important improvement concerns the block matching, based on straight Euclidean distance in the original algorithm. The ultimate goal of block matching is to find out the *signal* patches that most resemble the *signal* target patch. However, since the clean image is not available, at least in the first step, one can only work on *signal+noise* patches. Therefore, it can happen that some patches happen to be close to the target not because of an actual similarity of signal but as the effect of the random patterns of noise. This event, relatively uncommon in the AWGN case, can become a serious problem in the presence of strong correlated noise, when independent noise samples are reduced. If the noise is very structured and comparable in intensity with the signal it can dominate the block matching phase, leading to the selection

of patches loosely related (in terms of signal) with one another and, eventually, to a poor performance. Therefore, in nonlocal approaches it is very important to counter this problem. To this end, we carry out a prewhitening of the noisy image.

Let z be the observed noisy image, related to the noise-free image y by

$$z(n) = y(n) + h(n) * u(n) \quad (24)$$

where $u(n)$ is stationary white noise independent of $y(n)$, and $h(n)$ is a linear filter. The prewhitened image $z_{pw}(n)$ is then computed as the inverse transform of

$$Z_{pw}(\omega) = Z(\omega) \frac{1}{\max(\epsilon, |H(\omega)|)} \quad (25)$$

where $X(\omega)$ indicated discrete Fourier transform of $x(n)$, and ϵ is a small positive constant added to ensure stability. The prewhitened image is then used to locate the best matching patches, while all other processing steps take place on the original image.

It is worth underlining that this approach is quite different from that of Dabov et al. [83], let us call it BM3D-C, where no prewhitening is carried out but block similarity is computed in the transform domain with a weighted Euclidean distance, with smaller weights associated to noisier coefficients to reduce their detrimental effects.

On the contrary, for our second modification, concerning coefficient shrinkage, we follow closely the approach proposed by Dabov et al.. In particular, focusing on the first step of BM3D, we carry out hard-thresholding using a different threshold for each coefficient, proportional to the expected variance of noise. In formulas:

$$\lambda(i, j) = \lambda \sigma_{2D}(i) \quad (26)$$

where i and j are indexes associated with the 2D spatial and 1D transforms, respectively, and λ is a constant. By so doing, we increase our chances to suppress large coefficients originated exclusively by noise and, at the same time, to keep small coefficients with significant signal contribution. As for the variances, following the model in (24), they can be computed as:

$$\sigma_{2D}^2(i) = \frac{\sigma^2}{N_1^2} \left\| \left\| H(\omega) |F\{\psi_{T_{2D}}^{(i)}\} \right\|_2 \right\|_2^2 \quad (27)$$

where $\psi_{T_{2D}}^{(i)}$ is the i -th basis element of T_{2D} , $F\{\cdot\}$ indicates the discrete Fourier transform operator, σ^2 is the overall noise variance and N_1 is the block dimension.

Our last improvement concerns the empirical Wiener filtering in the second step which, just like hard thresholding in the first step, can be adapted to take into account the actual noise variances of coefficients according to

$$W(i, j) = \frac{\left| T_{3D}^{wie}(Y_{basic}^{z^T})(i, j) \right|^2}{\left| T_{3D}^{wie}(Y_{basic}^{z^T})(i, j) \right|^2 + \sigma_{2D}^2(i)} \quad (28)$$

where $\left| T_{3D}^{wie}(Y_{basic}^{z^T}) \right|^2(i, j)$ is the energy of the 3D transform coefficients of the basic estimate group where patches more similar to the target one P^T of z^T are collected. Here, we propose to estimate the variances $\sigma_{2D}^2(i)$ starting from the basic estimate of the clean image, \hat{y}_{basic} , provided by the first step. As a matter of facts, BM3D exploits the knowledge of \hat{y}_{basic} in the second step to accomplish several tasks: \hat{y}_{basic} is used to carry out the block matching process, which is why prewhitening is not required anymore, and also to obtain reliable estimates of signal statistics for the Wiener filtering. In the same manner, assuming

that \hat{y}_{basic} is a reliable estimate of the clean image y , the difference between the noisy image and the denoised one:

$$\hat{v}(n) = z(n) - \hat{y}_{basic}(n) \approx h(n) * u(n) \quad (29)$$

can be assumed to be a good estimate of the actual correlated noise. Therefore, by working on this noise image we can actually *measure* the coefficient noise variances, in each single group of blocks, rather than estimating them according to (27).

3.4. Results

In this section we describe the results of a limited set of experiments chosen to allow a comparison with reference techniques and highlight the major phenomena of interest.

In particular, we have simulated four type of colored noise: a bandpass noise with $\sigma=30$ on “House” image (Figure 3.6), and a line pattern noise like that found on analogue video with $\sigma=40$ on “Flinstones” image (Figure 3.7), exactly as they appear in the work of Goossens et al. [80]. In addition, we simulated two other type of colored noise, a bandpass noise with $\sigma=35$ on “House” image and a double line pattern noise with $\sigma=30$ on “House” image, as a further test of the efficacy of the proposed method.

Focusing on numerical results for House reported in Table 1, we note first of all that both NLM and BM3D degrade their performance as the noise becomes more structured, very likely because of the detrimental effects of noise on block matching.

TABLE 1: PSNR RESULTS FOR TEST IMAGES WITH FOUR TYPE OF SIMULATED CORRELATED NOISE.

	House ($\sigma=35$)	House ($\sigma=30$)		Flinstone ($\sigma=40$)
	band pass	band pass	stripes	stripes
Noisy image	17,25	18,59	18,59	16,09
NLM	26,68	28,51	26,67	22,51
BM3D	28,35	30,94	28,91	22,01
NLM-C	28,11	30,74	32,01	25,44
BM3D-C	28,77	31,44	30,78	23,63
Proposed	28,77	31,62	32,24	25,54

In all cases, BM3D keeps a 2dB edge *w.r.t.* NLM. Obviously, the colored-noise versions of the algorithms, NLM-C and BM3D-C, provide a significant gain *w.r.t.* the basic versions, especially for the case of more structured noise. It is worth underlining that the gain of NLM-C over NLM is much stronger than that of BM3D-C over BM3D, especially for structured noise. This backs up our conjecture that strong structured noise very much impairs block matching, and that the solution proposed by Dabov et al. [83] for BM3D-C does not really solve the problem.

Our proposed version of BM3D, which includes also improvements in the shrinkage phase and in the variance estimation, turns out to work well on very different types of noise, from one with granular aspects to streaked noise; unlike the other investigated methods appear to be effective only on particular type of correlated noise.

For example, the NLM-C performances are good on streaked noise, instead on band pass noise are even lower than BM3D-W developed in AWGN hypotheses. The reason for this behavior is probably due to noise spectral characteristics. The whitening operation before filtering is probably more “invasive”

for band pass noise than to others, altering the underlying signal characteristics, thereby reducing the denoising effectiveness.

On the contrary, BM3D-C returns better results for the band pass noise and only modest results for streaked noise. Despite the estimate transform coefficients variances are used in the block-matching to reduce the influence of noisier transform coefficients, probably the particular and repetitive pattern of streaked noise strongly influences the blocks distance measure. If the block matching is compromised, the remaining filtering part is ineffective.

Similar results are obtained for the Flinstone image with structured noise. The visual inspection of the filtered images of Figure 3.6 and Figure 3.7 further reinforces the positive judgement on the proposed algorithm, which removes most of the noise, like the other colored-noise algorithms, but presents a smaller number of ghost artifacts and of generally lower intensity.

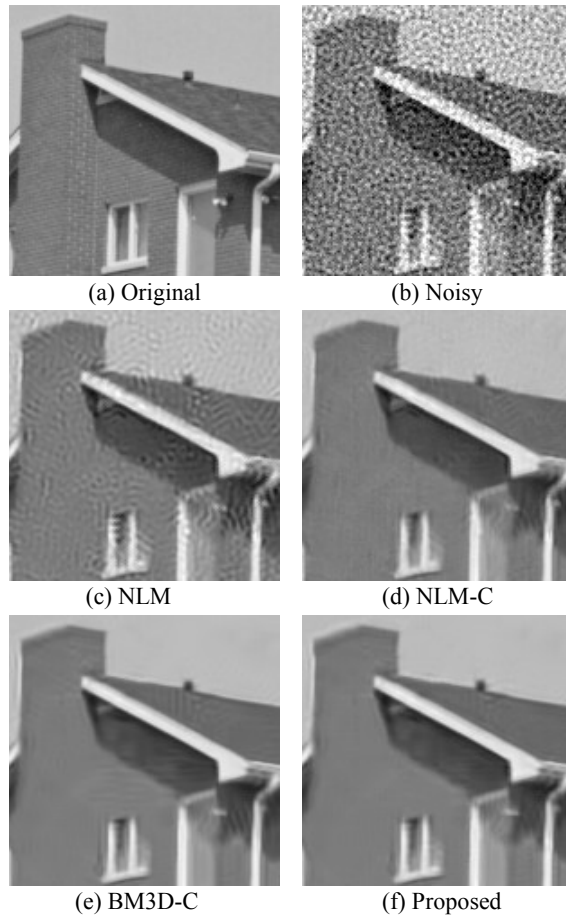


Figure 3.6: Visual results for a crop-outs of House.

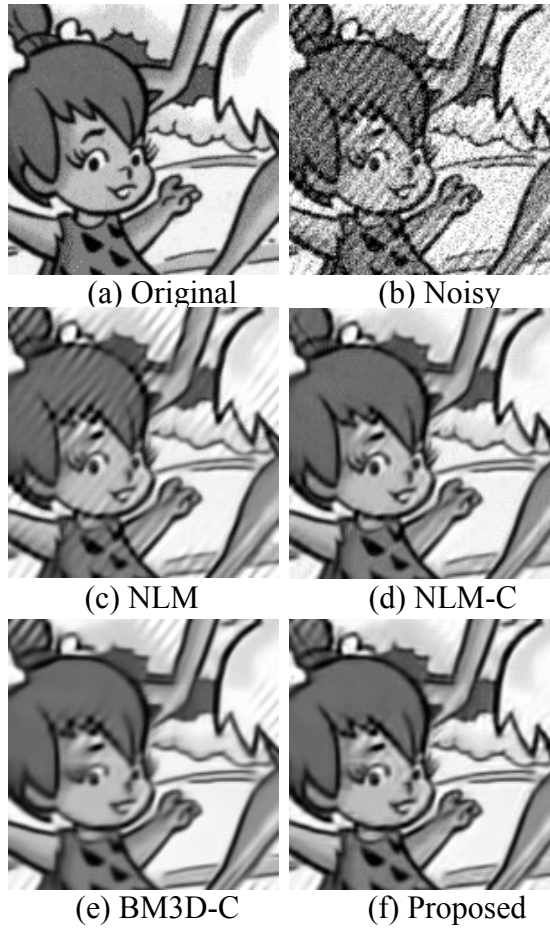


Figure 3.7: Visual results for a crop-outs of Flinestone.

Conclusion

In this thesis, we propose 3D algorithms for micro-architecture analysis based on the mathematical morphology theory. In particular, the *opening* operator properties have been exploited in the "successive openings" algorithm. It represents the starting point for the construction of three morphological synthetic indicators: the dimensional curves, the connectivity analysis, the effective porosity determination.

The dimensional curves return information about the pore or solid size distribution in a porous media. Applied to natural porous media, such as soils, this indicator allows to know their structural properties, and then to have some indications, for example, about the use of a soil in agriculture or about the physical and biological processes that determine its structure. A multi-modal pore size distribution, for example, indicates a highest heterogeneity of pores, that can be generally considered as a good indicator of soil physical quality, which can be related to, for instance, the plurality of habitats available for microbiological activity and to better effectiveness of water and air flow for the roots working. On the other hand, the trabecular size distributions of bone solid phase are powerful tools for diagnostic use. In particular, a unimodal pattern is associated with an homogeneous structure, while the presence of a large number of size classes is consistent with the bone sample affected by osteoporosis. This proves that the indicator we have proposed reflects the physiological or pathological nature of bone tissue samples. The connectivity curves, instead, allow to identify how the structural elements are interconnected. We have demonstrated that by connectivity analysis, it is also possible to identify the throat threshold value for the network. It is a critical diameter above which no connectivity and, then, no fluid passage is allowed anymore for the porous medium under

analysis. In particular, in biological application, this indicator shows that, for osteoporotic bone sample tissue, the connectivity is assigned to size classes smaller and less frequent than the varieties present in the volume. Finally, we have defined the effective porosity as the porosity fraction really interested in passage of fluids and we have implemented an efficient procedure for the automatic extraction of this component from to the total porosity. These results show that the proposed indicators together represent an effective tool for the porous media internal structure characterization.

Although “successive openings” is highly demanding in terms of CPU time, its fast version, based on the distance transform, provides still accurate results and is extremely fast.

The last part of our research is dedicated to reducing the strong noise that corrupts tomographic images. After evaluating experimentally the characteristics of noise, we propose a filtering technique for correlate noise based on the *Block-Matching 3D* (BM3D) algorithm. Experimental results on test images, corrupted by different types of colored noise, prove the effectiveness of the proposed technique.

Despite the micro-tomographic image processing presents considerable difficulties, both for the images intrinsic characteristics, and for the objects analyzed nature, in this thesis we have laid the foundations for a systematic study of the porous media structure, through the mathematical morphology theory. Certainly further investigations deserve issues such as micro-tomographic denoising and segmentation, which are only partially addressed in this work. They represent critical points in the micro-tomographic image processing, but present difficulties that require a great caution in deal with, altogether with a great research improvement.

References

- [1] D. Nield and A. Bejan, *Convection in porous media*. Springer Verlag, 2006.
- [2] W. B. Lindquist, "3dma general users manual," in *Stony Brook AMS Preprints*, 1999.
- [3] H. J. Vogel, "QuantIm C/C++ Library for Scientific image processing," 2010. [Online]. Available: http://www.higrade.ufz.de/data/quantim4_ref_manual8479.pdf.
- [4] R. A. Ketcham, "Computational methods for quantitative analysis of three-dimensional features in geological specimens," *Geosphere*, vol. 1, no. 1, p. 32, 2005.
- [5] A. Pierret, Y. Capowiez, L. Belzunces, and C. J. Moran, "3D reconstruction and quantification of macropores using X-ray computed tomography and image analysis," *Geoderma*, vol. 106, no. 3-4, pp. 247-271, Apr. 2002.
- [6] J. Serra, *Image analysis and mathematical morphology*. Academic Press, 1982, p. 610.
- [7] P. Maragos, A. Sofou, G. B. Stamou, V. Tzouvaras, E. Papatheodorou, and G. P. Stamou, "Image Analysis of Soil Micromorphology: Feature Extraction, Segmentation, and Quality Inference," *EURASIP Journal on Advances in Signal Processing*, vol. 2004, no. 6, pp. 902-912, 2004.

-
- [8] F. Mendoza, P. Verboven, H. K. Mebatsion, G. Kerckhofs, M. Wevers, and B. Nicolai, "Three-dimensional pore space quantification of apple tissue using X-ray computed microtomography.," *Planta*, vol. 226, no. 3, pp. 559-70, Aug. 2007.
- [9] A. Kaestner, "Imaging and image processing in porous media research," *Advances in Water Resources*, vol. 31, no. 9, pp. 1174-1187, Sep. 2008.
- [10] P. C. Baveye et al., "Observer-dependent variability of the thresholding step in the quantitative analysis of soil images and X-ray microtomography data," *Geoderma*, vol. 157, no. 1-2, pp. 51-63, Jun. 2010.
- [11] F. Terribile and E. FitzPatrick, "The application of multilayer digital image processing techniques to the description of soil thin sections," *Geoderma*, vol. 55, no. 1-2, pp. 159-174, 1992.
- [12] H. Yoon, C. Zhang, C. J. Werth, A. J. Valocchi, and A. G. Webb, "Numerical simulation of water flow in three dimensional heterogeneous porous media observed in a magnetic resonance imaging experiment," *Water Resources Research*, vol. 44, no. 6, pp. 1-12, 2008.
- [13] L. Tomutsa, D. Silin, and V. Radmilovic, "Analysis of chalk petrophysical properties by means of submicron-scale pore imaging and modeling," *SPE Reservoir Evaluation & Engineering*, vol. 10, no. 3, pp. 285-293, 2007.
- [14] H. Liu et al., "Three-Dimensional Orientation Mapping in the Transmission Electron Microscope," *Science*, vol. 332, no. 6031, p. 833, May. 2011.

-
- [15] B. Winkler et al., "Neutron imaging and neutron tomography as non-destructive tools to study bulk-rock samples," *European journal of mineralogy*, vol. 14, no. 2, pp. 349–354, 2002.
- [16] S. R. Stock, *Microcomputed tomography: Methodology and applications*. CRC, 2008.
- [17] A. C. Kak and M. Slaney, "Principles of computerized tomographic imaging," p. 329, 1988.
- [18] L. Feldkamp, L. Davis, and J. Kress, "Practical cone-beam algorithm," *JOSA A*, vol. 1, no. 6, pp. 612–619, 1984.
- [19] B. R. Whiting, P. Massoumzadeh, O. A. Earl, D. L. Snyder, and J. F. Williamson, "Properties of preprocessed sinogram data in x-ray computed tomography," *Medical physics*, vol. 33, no. 1, p. 3290, 2006.
- [20] G. Matheron, *Random sets and integral geometry*, vol. 9. Wiley New York, 1975.
- [21] G. Poggi and R. Ragozini, "Image segmentation by tree-structured Markov random fields," *Signal Processing Letters, IEEE*, vol. 6, no. 7, pp. 155–157, 1999.
- [22] R. A. Kerr, "Geologists Get Together to Dissect Earth's Thin Skin.," *Science (New York, N.Y.)*, vol. 262, no. 5136, pp. 992-3, Nov. 1993.
- [23] R. Costanza, R. D'Arge, R. D. Groot, and S. Farber, "The value of the world's ecosystem services and natural capital," *Nature*, 1997.
- [24] H. J. Vogel, "Morphological determination of pore connectivity as a function of pore size using serial

- sections,” *European Journal of Soil Science*, vol. 48, no. 3, pp. 365-377, Sep. 1997.
- [25] P. Bullock and C. P. Murphy, “Towards the quantification of soil structure.,” *Journal of Microscopy*, vol. 120, no. 3, pp. 317–328, 1980.
- [26] R. I. Al-Raoush and C. S. Willson, “Extraction of physically realistic pore network properties from three-dimensional synchrotron X-ray microtomography images of unconsolidated porous media systems,” *Journal of Hydrology*, vol. 300, no. 1-4, pp. 44-64, Jan. 2005.
- [27] J. Delerue, E. Perrier, A. Timmerman, and R. Swennen, “3D soil image characterization applied to hydraulic properties computation,” *Geological Society, London, Special Publications*, vol. 215, no. 1, pp. 167–176, 2003.
- [28] W. B. Lindquist, S. M. Lee, D. A. Coker, K. W. Jones, and P. Spanne, “Medial axis analysis of void structure in three-dimensional tomographic images of porous media,” *Journal of Geophysical Research*, vol. 101, no. 4, pp. 8297–8310, 1996.
- [29] T. C. Lee, R. L. Kashyap, and C. N. Chu, “Building skeleton models via 3-D medial surface/axis thinning algorithms,” *CVGIP: Graphical Model and Image Processing*, vol. 56, no. 6, pp. 462–478, 1994.
- [30] J. Thovert, J. Salles, and P. Adler, “Computerized characterization of the geometry of real porous media: their discretization, analysis and interpretation,” *Journal of microscopy*, vol. 170, no. 1, pp. 65–79, 1993.
- [31] J. D. Currey, *Bones: structure and mechanics*. Princeton Univ Pr, 2002.

- [32] R. Müller, M. Hahn, M. Vogel, G. Delling, and P. Rügsegger, "Morphometric analysis of noninvasively assessed bone biopsies: comparison of high-resolution computed tomography and histologic sections.," *Bone*, vol. 18, no. 3, pp. 215-20, Mar. 1996.
- [33] G. R. Davis and F. S. Wong, "X-ray microtomography of bones and teeth.," *Physiological measurement*, vol. 17, no. 3, pp. 121-46, Aug. 1996.
- [34] A. Laib, T. Hildebrand, H. J. Häuselmann, and P. Rügsegger, "Ridge number density: a new parameter for in vivo bone structure analysis.," *Bone*, vol. 21, no. 6, pp. 541-6, Dec. 1997.
- [35] J. Wolff, *The law of bone remodeling*. Springer-Verlag, 1986, p. xii, 126 p.
- [36] A. Parfitt, "Stereologic basis of bone histomorphometry: Theory of quantitative microscopy and reconstruction of the third dimension," *Bone histomorphometry: techniques and interpretation*, pp. 53-87, 1981.
- [37] B. Cortet, "Bone microarchitecture and mechanical resistance," *Joint Bone Spine*, vol. 68, no. 4, pp. 297-305, Jun. 2001.
- [38] E. Legrand et al., "Trabecular bone microarchitecture, bone mineral density, and vertebral fractures in male osteoporosis.," *Journal of bone and mineral research* □: *the official journal of the American Society for Bone and Mineral Research*, vol. 15, no. 1, pp. 13-9, Jan. 2000.
- [39] W. Whitehouse, "The quantitative morphology of anisotropic trabecular bone," *Journal of microscopy*, vol. 101, no. 2, pp. 153-168, 1974.

-
- [40] T. Hildebrand and P. Rügsegger, "Quantification of bone microarchitecture with the structure model index," *Computer Methods in Biomechanics and Bio Medical Engineering*, vol. 1, no. 1, pp. 15–23, 1997.
- [41] A. Odgaard, "Three-dimensional methods for quantification of cancellous bone architecture.," *Bone*, vol. 20, no. 4, pp. 315–28, Apr. 1997.
- [42] F. Meyer, "Mathematical morphology: from two dimensions to three dimensions," *Journal of microscopy*, vol. 165, no. 1, pp. 5–28, 1992.
- [43] G. W. Horgan, "Mathematical morphology for analysing soil structure from images," *European Journal of Soil Science*, vol. 49, no. 2, pp. 161–173, Jun. 1998.
- [44] A. J. H. Mehnert and P. T. Jackway, "On computing the exact euclidean distance transform on rectangular and hexagonal grids," *Journal of Mathematical Imaging and Vision*, vol. 11, no. 3, pp. 223–230, 1999.
- [45] C. Lantuejoul and F. Maisonneuve, "Geodesic methods in quantitative image analysis," *Pattern Recognition*, vol. 17, no. 2, pp. 177–187, 1984.
- [46] R. C. Gonzalez and R. E. Woods, *Digital image processing*, vol. 43, no. 11. Prentice Hall, 2008.
- [47] E. R. Dougherty and R. A. Lotufo, *Hands-on morphological image processing*, vol. 59. SPIE Press, 2003.
- [48] L. Vincent, "Watersheds in digital spaces: an efficient algorithm based on immersion simulations," *IEEE transactions on pattern analysis and machine*, pp. 583–598, 1991.

- [49] M. Matrecano, B. D. Matteo, and G. Mele, "3D imaging of soil pore network: two different approaches," in *EGU General Assembly*, 2009, vol. 11, pp. 10279-10279.
- [50] G. Mele, M. Matrecano, and S. Salatino, "Soil pore architecture and irrigation practices in vineyards: evaluation by X-ray micro-tomography," in *19th World Congress of Soil Science, Soil Solutions for a Changing World, 1 – 6 August 2010*, 2010, no. August, pp. 72-75.
- [51] M. Matrecano, G. Mele, and X. Wang, "Long term changes in soil structure of microbial crusts," in *skyscan.be*, 2009, pp. 123-124.
- [52] M. Tapiovaara and R. Wagner, "SNR and noise measurements for medical imaging: I. A practical approach based on statistical decision theory," *Physics in medicine and biology*, vol. 38, p. 71, 1993.
- [53] M. Sandborg, D. Dance, G. A. Carlsson, and J. Persliden, "Monte Carlo study of grid performance in diagnostic radiology: factors which affect the selection of tube potential and grid ratio," *British journal of radiology*, vol. 66, no. 792, p. 1164, 1993.
- [54] B. R. Whiting, "Signal statistics in x-ray computed tomography," in *Proceedings of SPIE*, 2002, vol. 4682, p. 53.
- [55] H. Lu, X. Li, I.-tsung Hsiao, and Z. Liang, "Analytical Noise Treatment for Low-Dose CT Projection Data by Penalized Weighted Least-Square Smoothing in the K-L Domain," *Physics*, vol. 4682, pp. 146-152, 2002.
- [56] D. A. Chesler, S. J. Riederer, and N. J. Pelc, "Noise due to photon counting statistics in computed x-ray

- tomography,” *Journal of Computer Assisted Tomography*, vol. 1, no. 1, p. 64, 1977.
- [57] G. T. Herman, “On the noise in images produced by computed tomography,” *Computer Graphics and Image Processing*, vol. 12, no. 3, pp. 271–285, 1980.
- [58] R. Huesman, “A new fast algorithm for the evaluation of regions of interest and statistical uncertainty in computed tomography,” *Physics in Medicine and Biology*, vol. 29, p. 543, 1984.
- [59] N. Alpert et al., “Estimation of the local statistical noise in emission computed tomography,” *IEEE Transactions on Medical Imaging*, vol. 1, no. 2, pp. 142–146, 2007.
- [60] S. J. Riederer, N. J. Pelc, and D. A. Chesler, “The noise power spectrum in computed X-ray tomography.,” *Physics in Medicine and Biology*, vol. 23, no. 3, pp. 446–454, 1978.
- [61] R. F. Wagner, D. G. Brown, and M. S. Pastel, “Application of information theory to the assessment of computed tomography,” *Med. Phys*, vol. 6, no. 2, pp. 83–94, 1979.
- [62] K. M. Hanson, “Detectability in computed tomographic images,” *Med. Phys*, vol. 6, no. 5, pp. 441–451, 1979.
- [63] K. Faulkner and B. Moores, “Analysis of x-ray computed tomography images using the noise power spectrum and autocorrelation function,” *Physics in Medicine and Biology*, vol. 29, no. 11, p. 1343, 1984.
- [64] J. H. Siewerdsen, I. a Cunningham, and D. a Jaffray, “A framework for noise-power spectrum analysis of

- multidimensional images,” *Medical Physics*, vol. 29, no. 11, p. 2655, 2002.
- [65] S. J. Tu, C. C. Shaw, and L. Chen, “Noise simulation in cone beam CT imaging with parallel computing,” *Physics in medicine and biology*, vol. 51, no. 5, pp. 1283-97, Mar. 2006.
- [66] H. W. Lilliefors, “On the Kolmogorov-Smirnov test for normality with mean and variance unknown,” *Journal of the American Statistical Association*, pp. 399–402, 1967.
- [67] P. Gravel, G. Beaudoin, and J. A. De Guise, “A method for modeling noise in medical images,” *Medical Imaging, IEEE Transactions on*, vol. 23, no. 10, pp. 1221–1232, 2004.
- [68] T. Lei and W. Sewchand, “Statistical approach to X-ray CT imaging and its applications in image analysis. I. Statistical analysis of X-ray CT imaging,” *Medical Imaging, IEEE Transactions on*, vol. 11, no. 1, pp. 53–61, 1992.
- [69] J. Wang et al., “An experimental study on the noise properties of x-ray CT sinogram data in Radon space,” *Physics in medicine and biology*, vol. 53, no. 12, pp. 3327-41, Jun. 2008.
- [70] M. Matrecano, M. Poderico, G. Poggi, M. Romano, and M. Cesarelli, “Application of denoising techniques to micro-tomographic images,” in *Information Technology and Applications in Biomedicine (ITAB), 2010 10th IEEE International Conference on*, 2010, pp. 1-4.
- [71] K. L. Boedeker, V. N. Cooper, and M. F. McNitt-Gray, “Application of the noise power spectrum in modern diagnostic MDCT: part I. Measurement of noise power

- spectra and noise equivalent quanta.,” *Physics in medicine and biology*, vol. 52, no. 14, pp. 4027-46, Jul. 2007.
- [72] D. Donoho and J. M. Johnstone, “Ideal spatial adaptation by wavelet shrinkage,” *Biometrika*, vol. 81, no. 3, p. 425, 1994.
- [73] D. L. Donoho, “Denoising by soft-thresholding,” *IEEE Transactions on Information Theory*, vol. 41, no. 3, pp. 613-627, Jan. 1995.
- [74] M. S. Crouse, R. D. Nowak, and R. G. Baraniuk, “Wavelet-based statistical signal processing using hidden Markov models,” *Signal Processing, IEEE Transactions on*, vol. 46, no. 4, pp. 886–902, 1998.
- [75] A. Buades, B. Coll, and J. M. Morel, “A Review of Image Denoising Algorithms, with a New One,” *Multiscale Modeling & Simulation*, vol. 4, no. 2, p. 490, 2005.
- [76] K. Dabov, A. Foi, V. Katkovnik, and K. Egiazarian, “Image denoising by sparse 3-D transform-domain collaborative filtering.,” *IEEE transactions on image processing: a publication of the IEEE Signal Processing Society*, vol. 16, no. 8, pp. 2080-95, Aug. 2007.
- [77] M. Poderico, S. Parrilli, G. Poggi, and L. Verdoliva, “Sigmoid shrinkage for BM3D denoising algorithm,” in *Multimedia Signal Processing (MMSP), 2010 IEEE International Workshop on*, 2010, pp. 423–426.
- [78] S. Parrilli, M. Poderico, C. V. Angelino, G. Scarpa, and L. Verdoliva, “A nonlocal approach for SAR image denoising,” in *Geoscience and Remote Sensing Symposium (IGARSS), 2010 IEEE International*, 2010, pp. 726–729.

-
- [79] S. Parrilli, M. Poderico, C. V. Angelino, and L. Verdoliva, "A Nonlocal SAR Image Denoising Algorithm Based on LLMMSE Wavelet Shrinkage," *Geoscience and Remote Sensing, IEEE Transactions on*, no. 99, pp. 1–11, 2011.
- [80] B. Goossens, Q. Luong, A. Pizurica, and W. Philips, "An improved non-local denoising algorithm," in *Local and Non-Local Approximation in Image Processing, International Workshop, Proceedings*, 2008, p. 143.
- [81] J. Portilla, V. Strela, M. J. Wainwright, and E. P. Simoncelli, "Image denoising using scale mixtures of Gaussians in the wavelet domain.," *IEEE transactions on image processing*, vol. 12, no. 11, pp. 1338-51, Jan. 2003.
- [82] B. Goossens, A. Pizurica, and W. Philips, "Image denoising using mixtures of projected Gaussian scale mixtures," *Image Processing, IEEE Transactions on*, vol. 18, no. 8, pp. 1689–1702, Aug. 2009.
- [83] K. Dabov, A. Foi, V. Katkovnik, and K. Egiazarian, "Image restoration by sparse 3D transform-domain collaborative filtering," in *SPIE Electronic Imaging*, 2008, vol. 213462, no. 213462, pp. 681207-681207-12.